



# **ADVCOMP 2019**

The Thirteenth International Conference on Advanced Engineering Computing  
and Applications in Sciences

ISBN: 978-1-61208-737-5

September 22 - 26, 2019

Porto, Portugal

## **ADVCOMP 2019 Editors**

Claus-Peter Rückemann, Leibniz Universität Hannover / Westfälische  
Wilhelms-Universität Münster / North-German Supercomputing Alliance  
(HLRN), Germany

# ADVCOMP 2019

## Forward

The Thirteenth International Conference on Advanced Engineering Computing and Applications in Sciences (ADVCOMP 2019), held between September 22-26, 2019 in Porto, Portugal, continued a series of events meant to bring together researchers from the academia and practitioners from the industry in order to address fundamentals of advanced scientific computing and specific mechanisms and algorithms for particular sciences.

With the advent of high performance computing environments, virtualization, distributed and parallel computing, as well as the increasing memory, storage and computational power, processing particularly complex scientific applications and voluminous data is more affordable. With the current computing software, hardware and distributed platforms effective use of advanced computing techniques is more achievable.

The conference provided a forum where researchers were able to present recent research results and new research problems and directions related to them. The conference sought contributions presenting novel research in all aspects of new scientific methods for computing and hybrid methods for computing optimization, as well as advanced algorithms and computational procedures, software and hardware solutions dealing with specific domains of science.

The conference had the following tracks:

- Computing applications in science
- Computing mechanisms and methods
- Multidisciplinary Mobile and Web Applications in Modern Life

We take here the opportunity to warmly thank all the members of the ADVCOMP 2019 technical program committee, as well as all the reviewers. The creation of such a high quality conference program would not have been possible without their involvement. We also kindly thank all the authors that dedicated much of their time and effort to contribute to ADVCOMP 2019. We truly believe that, thanks to all these efforts, the final conference program consisted of top quality contributions.

We also gratefully thank the members of the ADVCOMP 2019 organizing committee for their help in handling the logistics and for their work that made this professional meeting a success.

We hope that ADVCOMP 2019 was a successful international forum for the exchange of ideas and results between academia and industry and to promote further progress in the field of engineering computing and applications in sciences. We also hope that Porto provided a pleasant environment during the conference and everyone saved some time to enjoy the historic charm of the city.

## **ADVCOMP 2019 Chairs**

### **ADVCOMP Steering Committee**

Juha Röning, University of Oulu, Finland  
Paul Humphreys, Ulster University, UK  
Wasif Afzal, Mälardalen University, Sweden  
Hans-Joachim Bungartz, TUM, Germany  
Andreas , Technische Universität Clausthal, Germany  
Ivan Rodero, Rutgers University - Piscataway, USA  
Dean Vucinic, Vrije Universiteit Brussel (VUB), Belgium | FERIT, Croatia,  
Wenbing Zhao, Cleveland State University, USA  
Rudolf Berrendorf, Bonn-Rhein-Sieg University, Germany

### **ADVCOMP Industry/Research Advisory Committee**

Yuri Alexeev, Argonne National Laboratory, USA  
Marcin Hojny, AGH University of Science and Technology, Kraków, Poland  
Alice Koniges, Lawrence Berkeley Laboratory/NERSC, USA  
Marcin Paprzycki, Systems Research Institute, Polish Academy of Sciences, Poland  
Folker Meyer, Argonne National Laboratory Computation Institute and Medical School |  
University of Chicago, USA  
Jian Lin, Huawei Technologies Co. Ltd, Hangzhou, China  
Simon Tsang, Vencore Labs Inc., USA  
Robert Clay, Sandia National Labs, USA  
Alfred Geiger, T-Systems Solutions for Research GmbH, Germany  
Hugo Daniel Meyer, University of Amsterdam, Netherlands

## **ADVCOMP 2019**

### **COMMITTEE**

#### **ADVCOMP Steering Committee**

Juha Röning, University of Oulu, Finland  
Paul Humphreys, Ulster University, UK  
Wasif Afzal, Mälardalen University, Sweden  
Hans-Joachim Bungartz, TUM, Germany  
Andreas , Technische Universität Clausthal, Germany  
Ivan Rodero, Rutgers University - Piscataway, USA  
Dean Vucinic, Vrije Universiteit Brussel (VUB), Belgium | FERIT, Croatia,  
Wenbing Zhao, Cleveland State University, USA  
Rudolf Berrendorf, Bonn-Rhein-Sieg University, Germany

#### **ADVCOMP Industry/Research Advisory Committee**

Yuri Alexeev, Argonne National Laboratory, USA  
Marcin Hojny, AGH University of Science and Technology, Kraków, Poland  
Alice Koniges, Lawrence Berkeley Laboratory/NERSC, USA  
Marcin Paprzycki, Systems Research Institute, Polish Academy of Sciences, Poland  
Folker Meyer, Argonne National Laboratory Computation Institute and Medical School | University of Chicago, USA  
Jian Lin, Huawei Technologies Co. Ltd, Hangzhou, China  
Simon Tsang, Vencore Labs Inc., USA  
Robert Clay, Sandia National Labs, USA  
Alfred Geiger, T-Systems Solutions for Research GmbH, Germany  
Hugo Daniel Meyer, University of Amsterdam, Netherlands

#### **ADVCOMP 2019 Technical Program Committee**

Waleed H. Abdulla, University of Auckland, New Zealand  
Mohamed Riduan Abid, Alakhawayn University, Morocco  
Wasif Afzal, Mälardalen University, Sweden  
Ayaz Ahmad, COMSATS University Islamabad, Wah Campus, Pakistan  
Francisco Airton Silva, Federal University of Piauí, Brazil  
Yuri Alexeev, Argonne National Laboratory, USA  
Sónia Maria Almeida da Luz, Polytechnic Institute of Leiria, Portugal  
Daniel Andresen, Kansas State University, USA  
Omar Andres Carmona Cortes, Instituto Federal do Maranhão, Brazil  
Alberto Antonietti, Politecnico di Milano, Italy  
Ehsan Atoofian, Lakehead University, Canada  
Abdel-Hameed Badawy, New Mexico State University & Los Alamos National Laboratory, USA  
Doo-Hwan Bae, School of Computing - KAIST, Korea  
Jorge Barbosa, Universidade do Porto, Portugal

Carlos Becker Westphall, University of Santa Catarina, Brazil  
R. Ben Djemaa, Institut Supérieur d'Informatique et des Techniques de Communication, Tunisia  
Rudolf Berrendorf, Bonn-Rhein-Sieg University, Germany  
Md Zakirul Alam Bhuiyan, Fordham University, USA  
Tekin Bicer, Argonne National Laboratory, USA  
Muhammad Naufal Bin Mansor, University Malaysia Perlis, Malaysia  
Kai Bu, Zhejiang University, China  
Pedro H. Bugatti, Federal University of Technology - Paraná (UTFPR), Brazil  
Hans-Joachim Bungartz, TUM, Germany  
Maxwell Cai, Leiden University, Netherlands  
Xiao-Chuan Cai, University of Colorado Boulder, USA  
Laura Carrington, PMAc Labs - SDSC/UCSD / EP Analytic Inc., USA  
Metec Celik, Erciyes University, Turkey  
Hsi-Ya Chang, National Center for High-performance Computing, Taiwan  
Huangke Chen, National University of Defense Technology, China  
Huixiang Chen, University of Florida, USA  
Liang Chen, University of West London, UK  
Robert Clay, Sandia National Labs, USA  
Christian Contarino, University of Trento, Italy  
Juan Manuel Corchado Rodríguez, University of Salamanca, Spain  
Andrews Cordolino Sobral, University of La Rochelle, France  
Gianpiero Costantino, IIT - CNR, Italy  
Subhro Das, IBM T.J. Watson Research Center, New York, USA  
Marisa da Silva Maximiano, Polytechnic of Leiria, Portugal  
Marcelo de Paiva Guimarães, Federal University of São Paulo, Brazil  
Daniele De Sensi, University of Pisa, Italy  
Vassilios V. Dimakopoulos, University of Ioannina, Greece  
Mohammed Nabil El Korso, Paris X University, France  
Maha Elarbi, University of Tunis (ISG-Campus), Tunisia  
Mahdi Esfahanian, Florida Atlantic University, USA  
Javier Fabra, Universidad de Zaragoza, Spain  
Tiziano Fagni, Institute of Informatics and Telematics (IIT) - CNR, Pisa, Italy  
Ali Farhadi, University of Memphis, USA  
Akemi Galvez Tomida, University of Cantabria, Spain  
Marc Gamell, Intel Corporation, USA  
Félix J. García Clemente, University of Murcia, Spain  
Leonardo Garrido, Tecnológico de Monterrey, Mexico  
Filippo Gaudenzi, Università degli Studi di Milano, Italy  
Alfred Geiger, T-Systems Solutions for Research GmbH, Germany  
Mahsa Ghasemi, The University of Texas at Austin, USA  
J. Paul Gibson, Telecom Sud Paris, France  
Jing Gong, KTH Royal Institute of Technology, Sweden  
Teofilo Gonzalez, University of California Santa Barbara, USA  
Bernard Grabot, LGP-ENIT, France  
Jerzy Grzymala-Busse, University of Kansas, USA  
Jagadeesh Gunda, University of Edinburgh, UK  
Yanfei Guo, MCS Division | ANL, USA  
Maki Habib, American University in Cairo, Egypt

Shaza Hanif, Higher Colleges of Technology, Sharjah, United Arab Emirates  
Abolfazl Hashemi, University of Texas at Austin, USA  
Houcine Hassan, Universidad Politécnica de Valencia, Spain  
Mohd Helmy Abd Wahab, Universiti Tun Hussein Onn Malaysia, Malaysia  
Marcin Hojny, AGH University of Science and Technology, Kraków, Poland  
Wladyslaw Homenda, Warsaw University of Technology, Poland  
Tzung-Pei Hong, National University of Kaohsiung, Taiwan  
Paul Humphreys, Ulster University, UK  
Andres Iglesias, University of Cantabria, Spain / Toho University, Japan  
Hiroshi Ishikawa, Tokyo Metropolitan University, Japan  
Koteswar Rao Jerripothula, Nanyang Technological University, Singapore  
Yiming Ji, University of South Carolina Beaufort, USA  
Zheming Jin, Argonne National Lab, USA  
Eugene John, The University of Texas at San Antonio, USA  
Lizy John, UT Austin, USA  
Kyungtae Kang, Hanyang University, Korea  
Attila Kertesz, University of Szeged, Hungary  
Jie Kong, Xi'an Shiyong University, China  
Alice Koniges, Lawrence Berkeley Laboratory/NERSC, USA  
Harald Köstler, Friedrich-Alexander University Erlangen-Nürnberg, Germany  
Leszek Koszalka, Wroclaw University of Science and Technology, Poland  
Pan Lai, Nanyang Technological University, Singapore  
Kartik Lakhotia, University of Southern California, USA  
Seyong Lee, Oak Ridge National Laboratory, USA  
Maurizio Leotta, University of Genova, Italy  
Clement Leung, The Chinese University of Hong Kong, Hong Kong  
Clement Leung, The Chinese University of Hong Kong, Hong Kong  
Jiajia Li, Georgia Institute of Technology, USA  
Jian Li, University of Massachusetts Amherst, USA  
Yiheng Liang, Bridgewater State University, USA  
Jian Lin, Huawei Technologies Co. Ltd, Hangzhou, China  
Chin-Jung Liu, Michigan State University, USA  
Glenn Luecke, Iowa State University, USA  
Emilio Luque, University Autònoma of Barcelona (UAB), Spain  
Stephane Maag, Telecom SudParis, France  
Elbert E. N. Macau, Instituto Nacional de Pesquisas Espaciais – INPE, Brazil  
Frederic Magoules, CentraleSupélec | Université Paris-Saclay, France  
Parikshit Maini, IIIT-Delhi, India  
Shikharesh Majumdar, Carleton University, Canada  
Laci Mary Manhães, Public University of Navarre, Spain  
Claudia Marcos, ISISTAN Research Institute | UNICEN University, Argentina  
Marcin Markowski, Wroclaw University of Science and Technology, Poland  
Alessandro Margara, Politecnico di Milano, Italy  
Cleyton Mário de Oliveira Rodrigues, University of Pernambuco, Brazil  
Piyush Mehrotra, NASA Ames Research Center, USA  
Gabriele Mencagli, University of Pisa, Italy  
Folker Meyer, Argonne National Laboratory Computation Institute and Medical School | University of Chicago, USA

Hugo Daniel Meyer, University of Amsterdam, Netherlands  
Mariofanna Milanova, University of Arkansas at Little Rock, USA  
Subrata Mitra, Adobe Research, India  
Ilya Moiseenko, Cisco Systems, USA  
Sébastien Monnet, University Savoie Mont Blanc, France  
Vadim Mottl, Computing Center of the Russian Academy of Sciences / Moscow Institute of Physics and Technology, Russia  
Laurent Nana, Université de Bretagne Occidentale, France  
Elena Maria Navarro Martinez, Universidad de Castilla-La Mancha, Spain  
Sarah Odofoin, Northumbria University, UK  
Joanna Isabelle Olszewska, University of West Scotland, UK  
Marcin Paprzycki, Systems Research Institute, Polish Academy of Sciences, Poland  
Prantosh Kumar Paul, Raiganj University, West Bengal, India  
Agostino Poggi, Università degli Studi di Parma, Italy  
Swaroop Pophale, Oak Ridge National Laboratory, USA  
Sumit Purohit, Pacific Northwest National Laboratory, USA  
Ahmad Rafi Qawasmeh, The Hashemite University, Jordan  
Andreas Rausch, Technische Universität Clausthal, Germany  
Diego P. Ruiz, University of Granada, Spain  
Kwangjin Park, Wonkwang University, South Korea  
Sonia Pérez Díaz, University of Alcalá, Spain  
Radu-Emil Precup, Politehnica University of Timisoara, Romania  
Shuhui Qu, Center for Sustainable Development and Global Competitiveness -Stanford University, USA  
Vaibhav Rastogi, University of Wisconsin, USA  
Javed Razzaq, Bonn-Rhein-Sieg University of Applied Sciences, Germany  
Barbara Re, University of Camerino, Italy  
Carlos Reaño, Queen's University Belfast, UK  
Michele Risi, University of Salerno, Italy  
Ivan Rodero, Rutgers University - Piscataway, USA  
Juha Röning, University of Oulu, Finland  
Swarup Roy, North-Eastern Hill University, India  
Julio Sahuquillo, Universitat Politècnica de Valencia, Spain  
Subhash Saini, NASA, USA  
Sebastiano Fabio Schifano, Università di Ferrara, Italy  
Erich Schweighofer, University of Vienna, Austria  
Alireza Shahrabi, Glasgow Caledonian University, UK  
Justin Y. Shi, Temple University, USA  
Philip Shilane, Dell EMC, USA  
Neha Shreya, Indian Institute of Tourism and Travel management, Noida, India  
Min Si, Argonne National Laboratory, USA  
Sören Sonntag, Intel, Germany  
Francesco Spegni, Università Politecnica delle Marche, Italy  
Giandomenico Spezzano, ICAR-CNR | University of Calabria, Italy  
Emanuele Storti, Università Politecnica delle Marche, Italy  
Yulei Sui, University of New South Wales (UNSW), Australia  
Yifan Sun, Technicolor Research, Los Altos, California  
Andrei Tchernykh, CICESE Research Center, Mexico  
Priscila Tiemi Maeda Saito, Federal University of Technology - Paraná (UTFPR-CP), Brazil

Jesmin Jahan Tithi, Intel Corp., USA  
Simon Tsang, Perspecta Labs, USA  
Costas Vassilakis, University of the Peloponnese, Greece  
Adriano Velasque Werhli, Universidade Federal do Rio Grande - FURG, Brazil  
Flavien Vernier, Université Savoie Mont Blanc, France  
Juan Vicente Capella Hernández, Universitat Politècnica de València, Spain  
Dario Vieira, EFREI, France  
Konstantinos Votis, Information Technologies Institute | Centre for Research and Technology Hellas, Thessaloniki, Greece  
Dean Vucinic, Vrije Universiteit Brussel (VUB), Belgium | FERIT, Croatia  
Guodong Wang, South Dakota School of Mines and Technology, USA  
Yanshan Wang, Mayo Clinic, Rochester, USA  
Yunsheng Wang, Kettering University, USA  
Xianglin Wei, Nanjing Telecommunication Technology Research Institute, China  
Gabriel Wittum, Goethe University Frankfurt, Germany  
Hui Wu, The University of New South Wales, Australia  
Mudasser F. Wyne, National University, USA  
Qiao Xiang, Yale University, USA  
Cong-Cong Xing, Nicholls State University, USA  
Zhijie Xu, University of Huddersfield, UK  
Feng Yan, University of Nevada, Reno, USA  
Xu Yang, Illinois Institute of Technology, Chicago, USA  
Yingzhen Yang, Snap Research, Australia  
Xiaodong Yu, Virginia Tech, USA  
Quan Yuan, University of Texas of the Permian Basin, USA  
Michael Zapf, University of Applied Sciences Nuremberg, Germany  
Vesna Zeljkovic, Lincoln University, USA  
Jianping Zeng, University of Nebraska-Lincoln, USA  
Ruo Chen Zeng, Marvell Semiconductor, USA  
Jie Zhang, Amazon AWS, USA  
Na Zhang, VMware Inc., USA  
Wenbing Zhao, Cleveland State University, USA

## Copyright Information

For your reference, this is the text governing the copyright release for material published by IARIA.

The copyright release is a transfer of publication rights, which allows IARIA and its partners to drive the dissemination of the published material. This allows IARIA to give articles increased visibility via distribution, inclusion in libraries, and arrangements for submission to indexes.

I, the undersigned, declare that the article is original, and that I represent the authors of this article in the copyright release matters. If this work has been done as work-for-hire, I have obtained all necessary clearances to execute a copyright release. I hereby irrevocably transfer exclusive copyright for this material to IARIA. I give IARIA permission to reproduce the work in any media format such as, but not limited to, print, digital, or electronic. I give IARIA permission to distribute the materials without restriction to any institutions or individuals. I give IARIA permission to submit the work for inclusion in article repositories as IARIA sees fit.

I, the undersigned, declare that to the best of my knowledge, the article does not contain libelous or otherwise unlawful contents or invading the right of privacy or infringing on a proprietary right.

Following the copyright release, any circulated version of the article must bear the copyright notice and any header and footer information that IARIA applies to the published article.

IARIA grants royalty-free permission to the authors to disseminate the work, under the above provisions, for any academic, commercial, or industrial use. IARIA grants royalty-free permission to any individuals or institutions to make the article available electronically, online, or in print.

IARIA acknowledges that rights to any algorithm, process, procedure, apparatus, or articles of manufacture remain with the authors and their employers.

I, the undersigned, understand that IARIA will not be liable, in contract, tort (including, without limitation, negligence), pre-contract or other representations (other than fraudulent misrepresentations) or otherwise in connection with the publication of my work.

Exception to the above is made for work-for-hire performed while employed by the government. In that case, copyright to the material remains with the said government. The rightful owners (authors and government entity) grant unlimited and unrestricted permission to IARIA, IARIA's contractors, and IARIA's partners to further distribute the work.

## Table of Contents

Optimal Approximation for Multidimensional Nonlinear Point Data Sets <i>Rudolf Neydorf, Dean Vucinic, and Victor Poliakh</i>	1
A Localized Hybrid Penalization Method for Simultaneous Data Reconstruction and Biase Field Correction <i>Linghai Kong</i>	8
Irrigation Reservoir Modeling in Catchments without Measurements of Stream Flow <i>Milan Cisty, Veronika Soldanova, and Barbora Povazanova</i>	12
Code Verification of PECM with Strongly Discontinuous Flows <i>Zhibo Ma</i>	19
Uncertainty Quantification of Density Reconstruction in High-Energy X-ray Radiography <i>Haibo Xu and Xinge Li</i>	25
Multi-Factor Authentication for Public Displays using the Semantic Ambient Media Framework <i>David Bouck-Standen and Josefine Kipke</i>	30

# Optimal Approximation for Multidimensional Nonlinear Point Data Sets

Rudolf Neydorf  
Don State Technical University  
Rostov-on-Don, Russia  
e-mail: ranpro@mail.ru

Dean Vućinić  
Vrije Universiteit Brussel (VUB)  
Brussel, Belgium  
e-mail: dean.vucinic@vub.be

Victor Poliakh  
Don State Technical University  
Rostov-on-Don, Russia  
e-mail: silvervpoliyah@gmail.com

**Abstract**—The mathematical modelling of complex physical processes (objects) is based on the approximation of their experimental output variables (point data sets). It is well known that the respective mathematical models are multidimensional and significantly nonlinear, thus various mathematical methods were developed to approximate the experimental point data, each having its own inherent approximation advantages and disadvantages. However, these methods did not take into account the data structural and parametric characteristics, and thus motivated this research to develop a more universal approximation methodology to this kind of problem. The applied approximation method, named Cut-Glue Approximation, takes into account any data order and/or any nonlinear dependency based on 3 principles: fragmentation of the initial data approximated by known methods; high-precision analytical approximation of local fragments; multiplicative analytic fragmentation of local functions isolated in the factor space. This paper considers the second stage of the Cut-Glue Approximation - analytical approximation of local fragments. The direct advantage of this approximation is the resulting mathematical model differentiability, which enables their analytical investigation, appropriate for modelling complex dynamical systems.

*Keywords*-experimental data; fragments; math modeling; approximation; error; evolutionary-genetic algorithm; optimization; heuristic algorithms

## I. INTRODUCTION

In the process of scientific and technological progress for the majority of real technical and technological objects, the experimental construction of Mathematical Models (MM) and their study by computer simulation methods are the only effective methods for solving problems.

This is because, due to the lack of a priori knowledge, theoretical research methods are not available for such objects. In addition, in the presence of significant nonlinearities of the internal relationships of the input and output data, the dependences for these objects are not always amenable for manipulation by known numerical methods.

For example, when modelling the aerodynamic characteristics of aeronautical vehicles, researchers often encounter significant nonlinearity and ambiguity of the aerodynamic laws of their own movement and interaction

with the environment. For example, mechanical production processes, apparatuses of the chemical industry and land vehicles, have substantially nonlinear characteristics.

The experimental MM construction of such objects is the mathematical data processing task. The complexity of the approximation of such nonlinear dependences is obvious and can be the source of the significant errors. The errors reduction is achieved through the use of effective approaches based on the original array fragmentation of Experimental Data (ED). The effective approaches are the following: piecewise approximation [1][2], methods of spline functions [3][4], and also radial basis functions [5][6]. These approaches significantly increase the approximation accuracy when compared to the ED array methods as a whole (polynomial expansions [5]–[8], regression analysis [9], etc.). However, this excludes or makes it difficult for using them for the analytical MM transformation due to their conditional logical form.

One of the effective means of expanding the possibilities and increasing the effectiveness of experimental methods for constructing MM was a method oriented to a highly formalized approach by constructing MM for essentially nonlinear objects based on the ED conducted in active experiments. In a number of papers, starting from 2012, the Cut-Glue Approximation method (CGA) was developed [10][11][12][13]. It is based on the special multiplicative processing of individual MM dependency sections, fairly accurately approximated by analytical functions. The result of such processing is a function that describes only isolated (at each site) areas of their definition. With similar properties of these functions, subjected to multiplicative processing, it is admissible to additively combine them into a single function that has the MM object properties [3][8].

The CGA method includes the sequential execution of a number of stages: fragmentation of ED - partitioning an array into separate sections - fragments (FED), local approximation of each of the FED by a certain function and the multiplicative processing that follows it and the additive combination of these functions of the MM object under study [12][13]. In this case, the phase of local FED approximation [10][12], for the constructed MM, is decisive for the overall final quantitative accuracy.

However, despite the rather large number of publications on the topic [8][13] the absence of fundamental restrictions on the dimensionality of the simulated nonlinear

dependencies is missing, and they were mainly illustrated by examples applying the CGA method for objects not higher than the second order. This was partly due to the need to illustrate the transformations and simulation results. Within the framework of this problem (approximation), there are mathematical and technological difficulties. Therefore, a detailed analysis of the solution for the 3-dimensional problem and its influence on the model dimension and methods applied with the obtained results seem relevant. This paper is dedicated to this topic.

It is necessary to develop an algorithm for the mathematical modelling of ED fragments with fairly simple analytical functions in structure that allow variation of their structural complexity and supplement it with a search algorithm for supporting structural parametric optimization. The aggregate (hybrid) algorithm finds a mathematical model of minimal complexity for any ED fragment being of any dimension ensuring the specified fragment approximation accuracy.

Section 2 explains the possible options for defining the applied polynomial approximation and the method to compute the related regression coefficients. Section 3 describes the importance of structural and parametric optimization of the proposed polynomial approximation, and section 4 describes the structural and parametric searches enabling to find the optimal fragment model of experimental data. The respective example is described in Section 5, where the optimal structural and parametric representation for the 3<sup>rd</sup> dimensional fragment is computed.

## II. PERFORMANCE ALGORITHM FOR 3-DIMENSIONAL DATA FRACTURES IN CGA

The already published research results [10]-[13], performed during the development of the CGA method, as

$$\begin{aligned}
 Y(x) = & b_0 + b_1x_1 + \dots + b_nx_n + b_{11}x_1^2 + b_{12}x_1x_2 + b_{13}x_1x_3 + \dots + b_{1n}x_1x_n + b_{22}x_2^2 + \\
 & + b_{23}x_2x_3 + \dots + b_{2n}x_2x_n + \dots + b_{(n-1)n}x_{n-1}x_n + b_{nn}x_n^2 + b_{111}x_1^3 + b_{112}x_1^2x_2 + \dots \\
 & + b_{11n}x_1^2x_n + \dots + b_{122}x_1x_2^2 + \dots + b_{1nn}x_1x_n^2 + b_{222}x_2^3 + b_{223}x_2^2x_3 + \dots + b_{22n}x_2^2x_n + \dots \\
 & + b_{nnn}x_n^3 + b_{1111}x_1^4 + b_{1112}x_1^3x_2 + \dots + b_{111n}x_1^3x_n + b_{1122}x_1^2x_2^2 + b_{1123}x_1^2x_2x_3 + \dots, \quad (1)
 \end{aligned}$$

where  $b_{ijk\dots}$  – coefficients of a polynomial of the 4th degree with the 3rd dimensionality of the simulated dependence. Their indices indicate the variables to be multiplied. For example,  $b_{1123}$  – product multiplier  $(x_1x_1x_2x_3)$ ;  $x_i$  indexed independent variables of the experimental dependence under study.

The PP Universal Structure (PP US) applies 2 loops. The internal loop is used to explore different factors values,  $x_i$  of minimum to maximum index, as well as for the members of the same power order, and during their transition to a higher order. The outer loop ensures a consistent order increase to the next group of polynomial members starting from zero to

well as, numerous studies of the ED approximation problem [3][8], showed that to build Locally Approximating Functions (LAF), i.e. implementation of the phase of the FED approximation, it is appropriate to use a well-developed apparatus of classical regression analysis (CRA) [8][9]. In this case, the fragmentary nature of the approximation, which implies a not too large amount of experimental data included in the ED, makes it expedient to restrict oneself to methods of polynomial approximation. They guarantee both the analyticity of LAF and the regularity of its structure. The importance of the latter property will become clear from the further description of the problem.

The fragmentary nature of the approximation of the array of ED in the CGA method means that the number of components of its FED can be quite large, and the complexity of the LAF for each FED will depend both on its size by the amount of data and on the dimension of the ED. In other words, the complexity of the LAF in approximation on the basis of only an accuracy criterion can be very high. When combining a large number of complex LAF in a single MM, the complexity of the latter may be unacceptably high. This circumstance indicates the need to state and solve the problem of the structural-parametric optimization of each LAF, which, in turn, requires the regularity of their structure in order to be able to control its complexity.

The Power Polynomials (PP) have this property due to their regular structure, which allows to implement unambiguous algorithms for constructing joint ventures and their combinatorial variation. For the dependence of any dimension of PP has a canonical structure. The uniqueness of its complication relies on maintaining a clear sequence of the introduced members [13]. The following is an example of PP for a 3-dimensional fragment of experimental data:

the specified order, following after the exhaustion of combinatorial variants when multiplying factors.

This approach and the shape of PP simplify the formal evaluation and comparison of the PP complexity in respect to their structures. However, their use in the FED regression modelling complicates the finding of the optimal regression coefficients. One of the most simple and well-known simplification methods is the possibility of representing the nonlinear terms with PP arguments for the extended pseudo-linear factor space with a new vector modelling the conditionally independent variables of higher dimension:

$$q(\tilde{x}) = \sum_{i=0}^{\tilde{n}} \tilde{b}_i \cdot \tilde{x}_i = \sum_{i=0}^n b_i \cdot x_i + \sum_{i=n+1}^{\tilde{n}} \hat{b}_i \cdot \hat{x}_i \quad (2)$$

where  $\tilde{b}_i$  – pseudo-linear polynomial coefficients,  $\tilde{n}$ -th dimensional,  $\tilde{x}_i$  – generalized arguments of the dependency being investigated, including, as initial arguments  $x_i$ , so are the pseudo-arguments formed from them  $\hat{x}_i = \prod_n x_i$  which are replaced by the multiplicative nonlinearities of the power polynomial.

The calculation of the regression coefficients for the considered polynomial variant in the matrix equation is the CRA linear variant:

$$\tilde{b} = (X^T X)^{-1} X^T y, \quad (3)$$

giving only suboptimal solution. In (3)  $y - N_k$  - vector of values of the k-th FED;  $X$  -input matrix  $\tilde{x}_{ij}; j \in [1, N_k]$  and  $i$  - numbers of experiments that coincide with the numbers of pseudo-variables. Interdependence part  $\tilde{x}_i$  determines the calculated sub-optimal coefficients  $\tilde{b}_i$  with respect to the criterion used in CRA: in the Least Squares Method (LSM) - this criteria is only heuristic. Therefore, the non-quadratic criterion solves the problem successfully with a combinatorial approach.

It should be noted that the CRA apparatus is used in its standard form without any modification, since the obtained best approximation variant is performed with the structural-parametric optimization (STR), as explained in this paper follow up. The parametric sub-optimization of polynomial coefficients is solved by CRA for each structural variant of PP.

The developed software supports the first CGA method stage when approximating a fragmented ED with the approximating PP optimal or suboptimal variant. The low problem complexity is solved (the approximating PP dimension and order) applying the direct variants search. If the complexity of the problem results in an unacceptable computing time, then the heuristic search optimization algorithms is applied, as already proven themselves in such cases. Therefore, the developed EGA modifications are subject-oriented for the FED approximation.

### III. STRUCTURAL-PARAMETRIC OPTIMIZATION OF FED MATHEMATICAL MODEL

The need for not only parametric search, requires in addition the optimal structural variant search, due to the fact that all included components cannot provide the required accuracy, since the properties of some nonlinear functions contradict the nature of the experimental dependences. Such specific functions that approximate well the curvature of the FED hyper-surface are unknown in advance for each individual fragment. The universal structure definition of the approximation function, with sufficient variety of elementary functions and their forms becomes a problem. A full PP

meets this requirement. Within the search, first of all, it is necessary to identify its order m, which sets the data approximation accuracy, which is decreased when compared to the full polynomial of order m-1. In addition, the effective FP members search increases the approximation accuracy.

The advantage of using the regression PP resolves this problem, as its structure can be implemented by a regular mathematical record of the “mask” type, which represents the PP structure of the n<sup>th</sup> dimension and the m<sup>th</sup> degree (special digital code). This code is convenient for the FP structure, which has a similar dimension and degree. The initial arrangement of the FP elements corresponds to the combinatorial rules for increasing the indexes of coefficients described above. This corresponds to a structural and parametric increasing series of the polynomial coefficients, where the prime numbers 0, 1, 2 ... indicate the number of the multiplicative factor in the polynomial member. Their combination specifies all the factors constituting a member, and the number of nonzero numbers determines the order of PP. The code description example for the 4<sup>th</sup> order FP structure of the 3<sup>rd</sup> dimension follows:

$$\begin{aligned} &0,1,2,3,11,12,13,22, \\ &23,33,111,112,113,122,123,133, \\ &222,223, 233,333, \\ &1111,1112,1122,1123,1133, \\ &1222,1223,1233,1333,2222,2223, 2233,2333,3333 \end{aligned} \quad (4)$$

In (4) it is an enumeration of the terms of a fourth order polynomial of 3 dimensions, where “1” - corresponds to x1, “2” - corresponds to x2, “3” - corresponds to x3, “4” - corresponds to x4.

It should be noted, when approximating a fragment consisting of  $q$  elements by CRA methods, it is possible to describe it by a polynomial of the same order. The number of polynomial members is less than the number of members of the fragment  $p < q$ . Thus, the maximum possible order for the FED approximation is its structure order.

By varying the PP terms, the optimal structure search is made for the FED PP under consideration. The use of the NP-complete exhaustive search taking into consideration all the possible combinations for an incomplete polynomial is found unacceptable for the high-dimensional FED. Thus the subject-oriented modification of EGA is used, and implemented as a tool for the variation search of terms included in the resulting polynomial. It should be noted that the use of the combinatorial exhaustive search for all the possible PP combinations is possible, and only applicable to small dependence dimensions with a small polynomial order.

### IV. POLYNOMIALS APPROXIMATION FOR STRUCTURAL AND PARAMETRIC OPTIMIZATION

The structural optimization search to find the suboptimal structure variant is based on a criterion in respect to which its complexity is calculated. Therefore, to assess the PP complexity criterion, it is worth noting that this difficult task

requires additional research. Intuitively, as in our case, the MM complexity depends on a discrete components number that determines the polynomial structure. The known approaches for the discrete complexity estimation use of the so-called “complexity scale” [13], and in the present research, the assessment of the structure complexity could be based on 2 types of scales:

1. Heuristic, in which the quantitative components of the overall polynomial complexity are associated with its parameters, such as the number of members of the "symbols", the order of the member, etc., and are set by the developer or expert;
2. Theoretical or experimental estimate of time resources for calculating the resulting value of each PP member.

According to them, and on the formula proposed below, the structure complexity of the polynomial variant is calculated as follows:

$$E(P) = \sum_{i=1}^N e_i \times x_i \tag{5}$$

where P – PP structure under consideration;

N – full PP member’s number, which includes the maximum possible number of members to define the fragment;

e – estimate for the *i*<sup>th</sup> member listed in table 2;

x – indicator of the occurrence or non-occurrence of the *i*<sup>th</sup> member in the considered PP structure.

For the first approach, a scale was heuristically designed, see example given in Table 1 (2<sup>nd</sup> line). This scale is constructed for the 4<sup>th</sup> order FP having 2-dimensional dependency. In the second case, as shown in Table 1 (3<sup>rd</sup> and 4<sup>th</sup> line), the scale fixes the time resources for calculating each PP member. The calculation is performed on a large sample (> 100000) using the desktop computer (CPU Pentium (R) Dual-Core 2.10 GHz, RAM 3 GB).

The Microsoft Visual Studio (MVS) software development environment is used for the implementation in the C# programming language. This development environment enables measuring the computation time for each PP member operations.

In Table 1, the 2<sup>nd</sup> column shows the 4<sup>th</sup> order FP coefficients, in the 3<sup>rd</sup> column the heuristic complexity estimates are shown for each FP member, in the 4<sup>th</sup> and 5<sup>th</sup> column the computing time (measured in MVS) respectively the corresponding estimates for the (*t-estimate*) computing time for the 4<sup>th</sup> order FP members is shown.

TABLE I. POLYNOMIAL STRUCTURE HEURISTIC AND RESOURCE SCALES

N <sub>2</sub>	Member structure	Heuristic estimate	Ms	t-estimate
1	0	0,5	310	3,1
2	1	1	310	3,1
3	2	1	310	3,1
4	3	1	310	3,1
5	11	2	375	3,75

6	12	2	375	3,75
7	13	2	375	3,75
8	22	2	375	3,75
9	23	2	375	3,75
10	33	2	375	3,75
11	111	3	415	4,15
12	112	3	415	4,15
13	113	3	415	4,15
14	122	3	415	4,15
15	123	3	415	4,15
16	133	3	415	4,15
17	222	3	415	4,15
18	223	3	415	4,15
19	233	3	415	4,15
20	333	3	415	4,15
21	1111	4	480	4,8
22	1112	4	480	4,8
23	1113	4	480	4,8
24	1122	4	480	4,8
25	1123	4	480	4,8
26	1133	4	480	4,8
27	1222	4	480	4,8
28	1223	4	480	4,8
29	1233	4	480	4,8
30	1333	4	480	4,8
31	2222	4	480	4,8
32	2223	4	480	4,8
33	2233	4	480	4,8
34	2333	4	480	4,8
35	3333	4	480	4,8

V. MATHEMATICAL MODEL EXAMPLE FOR STRUCTURAL AND PARAMETRIC OPTIMIZATION

As example for the proposed structural-parametric approximation of the ED array fragment, the complex balloon movement is considered. The balloon total air resistance force (its vertical component) is simulated with its ascending velocity *v* (m/s), angle *α* (angle), and height *h*(m), adopting the following notation: *v* ~ *x*<sub>1</sub>; *α* ~ *x*<sub>2</sub>; *h* ~ *x*<sub>3</sub>.

The ED fragment, see Figure 1, contains 36 elements. The full 4<sup>th</sup> order polynomial for the 3-dimensional dependency modelling contains 35 terms. Therefore, the limit FP fragment order is 4. Thus, the fragment modelling with 36 elements that contains 35 polynomial members is not a statistically acceptable option, since it takes into account only one of the existing degrees of freedom, and this is not enough to evaluate the resulting model. However, it should

be noted that often the PP variants, having a smaller number of members (but larger number of freedom degrees) are better modelling the approximation fragment than the full polynomial having the maximum possible order. Therefore, the maximum PP structure order is chosen, since it allows the search for the best approximation accuracy. This is enabled

by varying its members, for example, using the combinatorial search algorithm, as described previously, and the search approach based on the modified EGA.

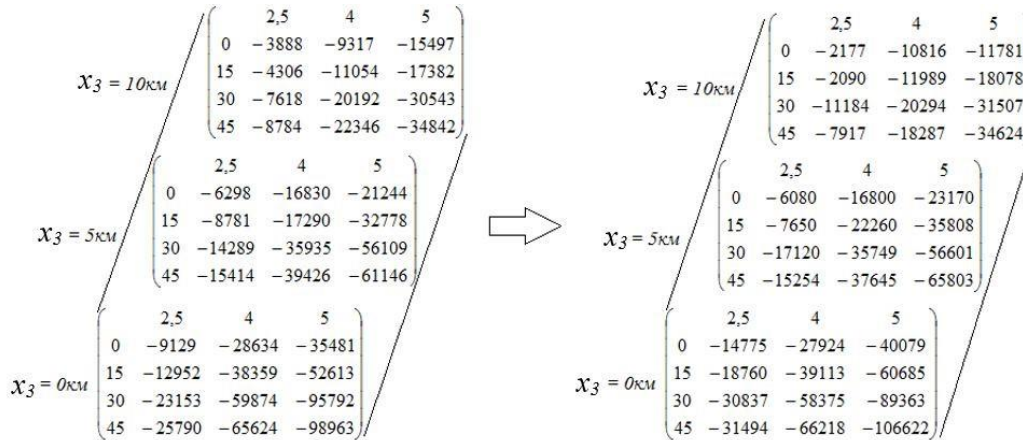


Figure 1: 3<sup>rd</sup> dimensional fragment results

To illustrate the 3-dimensional data source, we use a non-standard mathematical form writing. In the top rows and left columns of the ED matrices the fragments and the polynomial approximating it, see Figure 1, where the values  $x_1$  and  $x_2$  are shown. In the left part, the  $F_x$  (experimental data) matrix is shown, and in the right part, the analytically calculated values using STR are shown. The variation of the polynomial structure is carried out with the choice of PP variants satisfying the range of the ED relative error: 0.01–1% with a subsequent search in the resulting set of options for finding the minimal complexity structure.

Due to the fact that there is no universal and reliable theory of assessing the complexity of the joint, 2 types of criteria are proposed and validated: (1) Heuristic complexity scale, in which the polynomial members have assigned conditional estimate appropriate for their order and equal to it; (2) Considered to be more reasonable, since its complexity scale is based on the experimental estimates of the computational time for each PP member (see Table 1). By using them based on equation (5), the calculated structure complexity of the polynomial variant is shown.

The 4<sup>th</sup> order, PP members, with marks for their entry into the ranking of the 10 best structural-parametric polynomials

indicators are shown in columns of Table 2. The best PP options with relative error within specified limits are considered. In each column, "1" indicates the inclusion of the corresponding term in the final PP structure ( $z_i=1$ ), and the sign "-", on the contrary, indicates its exclusion from the final PP structure ( $z_i=0$ ). The bottom lines below these columns show the estimates for each option.

In Table 2, in the last 6 lines, the following notation is used:

- "Absolute error" and "Relative error" characterize the values of absolute and relative approximation errors;
- "Sum. 4" means the number of 4<sup>th</sup> order PP members is used as an additional criterion for assessing the complexity of the structure;
- "S1" denotes the total PP complexity based on the theoretical or experimental computational time estimates of the resulting value for each PP member;
- "S2" denotes the total PP complexity, based on the proposed heuristic scale;
- "SC" denotes the total PP complexity, based on 2 proposed scales.

TABLE II. RESULTS OF STRUCTURAL-PARAMETRIC OPTIMIZATION BASED ON THE PROPOSED DIFFICULTY SCALES

№ CII (i)	1	2	3	4	5	6	7	8	9	10
0	1	1	1	1	1	1	1	1	1	1
1	--	1	--	1	1	1	--	1	--	1
2	--	--	--	1	--	1	--	1	--	1
3	1	1	1	1	1	--	--	--	--	--
11	--	--	--	--	--	1	--	--	--	--
12	1	1	1	--	--	--	--	--	1	--
13	--	--	--	--	--	--	1	1	--	1
22	1	--	--	1	1	--	1	--	1	--
23	--	1	1	--	--	1	1	1	--	1
33	1	1	1	1	1	1	1	1	1	1
111	1	--	--	1	1	1	--	1	1	1
112	1	1	1	--	1	--	1	1	1	--
113	1	1	1	--	--	--	1	1	1	--
122	--	1	1	--	1	1	--	--	--	--
123	1	--	--	1	--	1	1	1	1	1
133	1	1	1	--	1	1	--	--	1	1
222	--	1	1	1	1	--	1	1	--	1
223	1	--	--	--	1	1	--	--	1	--
233	--	--	--	--	--	--	--	--	--	--
333	1	1	1	1	1	1	1	1	1	1
1111	1	--	--	--	--	1	1	--	1	--
1112	--	--	--	--	--	--	--	--	--	--
1113	--	1	1	1	1	--	--	1	--	1
1122	1	1	1	1	1	--	1	1	1	1
1123	1	1	1	1	1	--	1	1	1	1
1133	1	1	1	1	1	--	1	1	1	1
1222	--	--	--	--	--	--	--	--	--	--
1223	1	--	--	--	--	1	1	--	1	--
1233	1	--	--	--	--	1	1	--	1	--
1333	1	1	1	1	1	1	1	1	1	1
2222	--	--	--	--	--	--	--	--	--	--
2223	1	1	1	1	1	--	1	1	1	1
2233	--	--	--	--	--	--	--	--	--	--
2333	--	--	--	--	--	--	--	--	--	--
3333	--	--	--	--	--	--	--	--	--	--
Absolute error	6062,9	6243,7	6465,4	6498,4	6791	6918,4	7187	7262,6	8078,7	8138,3
Relative error	0,063	0,065	0,067	0,068	0,071	0,072	0,075	0,076	0,084	0,085
Sum. 4	7	9	9	9	9	11	7	8	7	9
S1	84,905	74,25	71,15	65,305	74,655	64,65	77,255	74,25	81,805	70,1
S2	60,5	50,5	49,5	43,5	51,5	42,5	55,5	50,5	59,5	47,5
SC	145,405	124,75	120,65	108,805	126,155	107,15	132,755	124,75	141,305	117,6

Rows S1, S2 and SC show the criteria values on the basis of which the PP structural complexity is estimated. In addition, the 4<sup>th</sup> order PP member's number is taken into account leading to a more complex structure.

The joint structure, which is shown in the 6<sup>th</sup> column for the accepted formulation, can be considered as an absolute structural-parametric optimum, since, with sufficient accuracy, it has the least structural complexity. It can be noted that PP, shown in the 1–5<sup>th</sup> columns, have an advantage over PP shown in the 6<sup>th</sup> column, in terms of the absolute and relative errors. However, PP in the 6<sup>th</sup> column is simpler than all the other 9 variations of the PP according to the 2 criteria formed in this

work (S1, S2) and includes only 4<sup>th</sup> order members, which joint includes 6 members of the 4<sup>th</sup> order, as shown in the 4<sup>th</sup> column.

## VI. CONCLUSION

The proposed coding pattern for the polynomial approximation structure provides the unified and efficient approach for the formulation of the universal MM for describing 1-st, 2-nd, and 3-dimensional data fragments. Moreover, the possibility of using the applied algorithm to increase the order for their large values is outside the scope of this research. The proposed MM-s for estimating the PP structural complexity make possible to perform their structural optimizations by applying any discrete methods opening up new possibilities in finding optimal approximations methods. The combined heuristic search for parametric optimization and the combinatorial algorithm for the polynomial structural optimization enable solving the conditional optimization problem of the subject-based criteria. The heuristic polynomial optimization algorithm improves the approximation accuracy, based on the EGA modification, which makes possible to find a suboptimal mathematical description of the high-dimensional fragments for which the use of a combinatorial optimization method is not an effective approach in terms of time costs. However, the plans still have a lot of work to finalize the proposed approach to the approximation of fragments, for example, filtering descriptions of FED regarding their behavior between the FED points.

## ACKNOWLEDGMENT

The research supporter by the Russian Foundation of Fundamental Research, project No. 18-08-01178/19 A

## REFERENCES

- [1] M. A. Ayzerman, Y. S. Pyatnitskiy Osnovy teorii razryvnykh sistem I [The fundamentals of the theory of discontinuous systems]. *Avtomatika i telemekhanika* [Automation and Remote Control], 1974, no. 7, pp. 33–47.
- [2] M. A. Ayzerman, Y. S. Pyatnitskiy Osnovy teorii razryvnykh sistem I [The fundamentals of the theory of discontinuous

- systems]. *Avtomatika i telemekhanika* [Automation and Remote Control], 1974, no. 8, pp. 39–61.
- [3] S. S. Tolstykh Matrichnyy kriteriy strukturnoy slozhnosti zamknutykh sistem [Matrix criterion for the structural complexity of closed systems]. *Vestnik Tambovskogo gosudarstvennogo tekhnicheskogo universiteta* [Bulletin of Tambov State Technical University], 1998, vol. 4, no. 2–3, pp. 238–244.
- [4] B. Douglas, D. Watts. *Nonlinear regression analysis and its applications*. New York, John Wiley & Sons, 1988. – 365 p.
- [5] N. R. Drapper, H. Smith *Applied regression analysis*. New York, John Wiley & Sons, 1981, vol. 1. 366 p.
- [6] N. R. Drapper, H. Smith *Applied regression analysis*. New York, John Wiley & Sons, 1981, vol. 2. 351 p.
- [7] R. C. Eberhart, J. A. Kennedy New optimizer, using particle swarm theory. *Proceedings of the 6th International Symposium on Micromachine and Human Science*. Japan, Nagoya, 1995, pp. 39–43.
- [8] J. O. Rawlings, G. P. Sastry and D. A. Dickey. *Applied Regression Analysis: A Research Tool*. 2nd ed. 1998.
- [9] J. Kennedy, R. Eberhart Particle Swarm Optimization. *Proceedings of IEEE International Conference on Neural Networks*. New Jersey, Piscataway, 1995, pp. 1942–1948.
- [10] R. Neydorf, I. Chernogorov and D. Vucinic Search Opportunities of Swarming Particles Methods in Irregular Multi-Extreme Environments. *Proceedings of the XI International Conference on Advanced Engineering Computing and Applications in Sciences ADVCOMP2017*. Spain, Barcelona, 2017, pp. 7–12.
- [11] R. Neydorf Bivariate "Cut-Glue" Approximation of Strongly Nonlinear Mathematical Models Based on Experimental Data. *SAE Int. J. Aerosp.*, 2015, no. 8 (1), pp. 47–54.
- [12] R. Neydorf, I. Chernogorov, V. Polyakh, O. Yarakhmedov, J. Goncharova J. and A. Neydorf Formal Characterization and Optimization of Algorithm for the Modelling of Strongly Nonlinear Dependencies Using the Method "Cut-Glue" Approximation of Experimental. *SAE Technical Paper* 2016-01-2033, 2016, pp. 1–12.
- [13] R. Neydorf, V. Polyakh, I. Chernogorov, O. Yarakhmedov and D. Vucinic "Cut-glue" approximation improvements with evolutionary-genetic algorithm for strongly nonlinear parametric dependencies of mathematical models. *Performance of Materials. Design and Experimental Approaches*. Springer, 2018, pp. 245-257. Available at: <https://link.springer.com/book/10.1007/978-3-319-59590-0/page/2>.
- [14] Y. Shi, R. C. Eberhart A modified particle swarm optimizer. *Proceedings of the IEEE Congress on Evolutionary Computation*. New Jersey, Piscataway, 1998, pp. 69–73

# A Localized Hybrid Penalization Method for Simultaneous Data Reconstruction and Bias Field Correction

Linghai Kong

Institute of Applied Physics and Computational Mathematics  
Beijing, PR China  
email: [kong\\_linghai@iapcm.ac.cn](mailto:kong_linghai@iapcm.ac.cn)

**Abstract**—A new variational model is dedicated to simultaneous image reconstruction and bias field rectification, where the image is corrupted by mixed Laplace-Gaussian noise. To solve the model numerically, an adaptive augmented Lagrangian method is combined with the expectation maximization strategy. Some numerical results are also presented to validate the proposed model and algorithm.

**Keywords**- Localized Regularization Method; Mixed Laplace-Gaussian Noise; ALM; EM; Data Reconstruction; Bias correction

## I. INTRODUCTION

This paper addresses the problem of rectifying bias field in images corrupted by mixed noise. Bias field, also known as intensity inhomogeneity, is the spurious smooth intensity variation across the whole image. It is present in many different imaging modalities, such as microscopy, ultrasound and Magnetic Resonance Imaging (MRI), and high-energy radiography (HER) as well (e.g., [1]). In HER, the bias field can be resulted in the intensity distribution of the radiation source, the artifact of the image intensifier and the vignetting effect of the optical lens in the charge-coupled-device (CCD) based imager. Many image analysis processes, including image segmentation and Abel inverse transformation, are highly sensitive to the issue.

In HER, the problem of image denoising has to be considered carefully. In CCD-recorded data, background hot noise is inherent in the current carriers, while pulse spike noise is also encountered due to not only the interaction between transmitted particles and CCD chips, but the tremendous flaw in the transistors as well. In other words, its statistical property is a combination of two different distributions. In this paper, we focus on a special case of noise distribution, that is, Laplace and Gaussian mixture (LGM). Our problem is then to reconstruct an original image from an observation with simultaneous LGM noise removal and bias field correction.

As it is known, finite mixture models are among the most familiar approaches for image segmentation and intensity inhomogeneity elimination (i.e., [2]). They combine the maximum likelihood (ML) or maximum a posterior (MAP) probability criterion with the expectation maximization (EM) algorithm to construct subjective energy functionals. Mixture noise models have also been drawn much research interest in the community of image processing, including Poisson-Gaussian noise and impulse-

Gaussian noise (e.g., [3]-[6]). Liu et al. [7] proposed a finite Laplacian mixture model to approximate the impulse noise. The authors combined the first order total variation (FOTV) regularization with the EM method to gain an adaptive restoration method. In [8], Gong, Shen and Toh present a first order regularization model to recover images contaminated by mixed or even unknown noises. More recently, Calatroni et al. [9] proposed a variational model encoding the mixed Poisson-Gaussian noise as an infimal convolution of discrepancy terms of noise distributions.

During the last two decades, numerous approaches have been suggested to correct the bias field, which are mainly divided into two categories. The first one is parameter algorithms, and the second one is non-parametric methods, which do not require any prior knowledge on the intensity probability distribution and the bias field is integrated into a faith energy based on ML or MAP estimation.

In this paper, we propose a variational method by integrating the LGM model with the EM algorithm to investigate the inverse problem in the presence of bias field and mixed noise. The data term in our energy is derived from a localized LGM assumption, and the bias field is regarded as a parameter of the LGM model. Compared with earlier methods based on mixture assumptions, our model contains a higher-order cost term [10], used to eliminate the staircasing fallback of the first-order total variation, and it does not require extra constraints on the bias field. Moreover, the regularization parameters in our model are updated adaptively according to the change of the functional cost. Numerical experiments on MRI images have shown its efficiency.

The remainder of the paper is organized as follows. Section 2 introduces the BiLGM-TVBH model based on the EM algorithm. Section 3 presents briefly the numerical algorithm of our proposed model and some experimental results. Concluding remarks are given in the last section.

## II. LGM MODEL AND EM ALGORITHM

Some notations adopted in this paper is listed as follows. Let  $\mathbb{R}^n$  be  $n$ -dimensional real Euclidean space,  $\mathbb{R} = \mathbb{R}^1$ . In the following, we denote  $u, f: \Omega \subset \mathbb{R}^2 \rightarrow \mathbb{R}$  to be an original gray scale image and an observed image describing the same scene,  $\Omega$  is open and bounded with Lipschitz boundary.

Assuming no blurring effect on the observed image, the reconstruction problem assumes the following form

$$\text{find } u \text{ s.t. } f(x) = b(x)(Hu(x) + n(x)), \quad (1)$$

where  $b, n: \Omega \rightarrow \mathbb{R}$  represent the bias field and the additive noise, respectively.  $H$  is a forward map, such as Abel's transform [11][12] given by

$$Hu(x) \cong Hu(s, t) = \int_{|s|}^{+\infty} \frac{ru(r, t)}{\sqrt{r^2 - |s|^2}} dr. \quad (2)$$

$n(x)$  is a realization of independent and identically distributed random variable  $\eta$  with PDF

$$p_\eta(z, \Theta_0) = \sum_{k=1}^2 \gamma_k p_k(z; \sigma_k^2), \quad (3)$$

$$p_1(z; \sigma_1^2) = \frac{1}{2\sigma_1^2} e^{-|z|/\sigma_1^2},$$

$$p_2(z; \sigma_2^2) = \frac{1}{\sqrt{2\pi\sigma_2^2}} e^{-|z|^2/\sigma_2^2},$$

$\Theta_0$  denotes the parameter set  $\{\sigma_k^2, \gamma_k, k = 1, 2\}$ ,  $\gamma_k$  is positive real number acting on mixture radio.

Following the idea in [13] and the references therein, the bias field function  $b(x)$  is assumed to be positive, smoothly varying function on the image domain  $\Omega$  such that  $b(s) \approx b(x)$  for all  $s \in O_x$  which is definitely small neighborhood with center at  $x$ . We regard the intensity of the observation is a realization of a random variable  $\xi$  for all  $x \in \Omega$ . Then, by routine computation, there holds

$$p_\xi(z; \Theta) = \frac{\gamma_1}{2b\sigma_1^2} e^{-\frac{|z-bHu|}{b\sigma_1^2}} + \frac{\gamma_2}{\sqrt{2\pi b^2\sigma_2^2}} e^{-\frac{|z-bHu|^2}{2b^2\sigma_2^2}} \quad (4)$$

with  $\Theta = \Theta_0 \cup b$ . And then, our problem is reformulated to reconstruct  $u$  from relation (1) with unknown parameter set  $\Theta$ .

Based on the framework of Bayesian approach [14][15], the MAP estimation of  $u$  can be given by

$$u^* = \arg \min_u \{-\log(f|u) - \log p(u)\} \quad (5)$$

that is,  $u^*$  minimizes an energy functional with two different components: the fidelity part,  $-\log p(f|u)$ , can be further specified by MAP estimation and EM algorithm; the penalty part,  $-\log p(u)$ , can be designated as the combination of the first and second order total variation [6],[10] for detail preserving and artifact elimination.

Making use of the expression (3) and the assumptions on the bias field function, all the intensities  $f(t)$  within a neighborhood  $O_s$  share the same PDF  $p_\xi(z, \Theta)$ . For simplification, we introduce some notations as follows.

$$w_1(s) = \frac{\gamma_1}{2b(s)\sigma_1^2}, w_2(s) = \frac{\gamma_2}{\sqrt{2\pi b^2(s)\sigma_2^2}},$$

and

$$g = g(x, s) = \left| \frac{f(x)}{b(s)} - Hu(x) \right|. \quad (6)$$

By the independency assumption, we have a local negative log-likelihood functional in the neighborhood

$$\mathcal{E}_s(\Theta, u) = - \int_{O_s} \log \left( w_1 e^{-\frac{g}{\sigma_1^2}} + w_2 e^{-\frac{g^2}{2\sigma_2^2}} \right) dx. \quad (7)$$

Then introduce a Gaussian weighting function to identify the contribution of different points in the neighborhood, the local energy becomes

$$\mathcal{E}_s(\Theta, u(s)) = - \int_{O_s} G_\sigma(s-x) \log \left( w_1 e^{-\frac{g}{\sigma_1^2}} + w_2 e^{-\frac{g^2}{2\sigma_2^2}} \right) dx. \quad (8)$$

where  $G_\sigma(\cdot)$  is a symmetric Gaussian kernel with a standard deviation  $\sigma$  such that  $G_\sigma(t) \approx 0$  as  $t \notin O_s$ .

Then, expanding the local integral domain to the whole domain  $\Omega$  and considering the global information of the given data, we have the following energy functional

$$\mathcal{E}(\Theta, u) = - \iint_{\Omega} G_\sigma \log \left( w_1 e^{-\frac{g}{\sigma_1^2}} + w_2 e^{-\frac{g^2}{2\sigma_2^2}} \right) dx ds. \quad (9)$$

To perform estimation on  $\Theta$ , we utilize the EM algorithm. Introducing a vector-valued auxiliary variable  $\varphi = (\varphi_1, \varphi_2)$  in

$$\Delta = \{\varphi | 0 < \varphi_i < 1, \sum_{i=1}^2 \varphi_i = 1\}, \quad (10)$$

and a functional

$$\Phi(\Theta, u, \varphi) = \iint G_\sigma \left( \frac{\varphi_1}{\sigma_1^2} g + \frac{\varphi_2}{2\sigma_2^2} g^2 - \varphi_1 \log \frac{\gamma_1}{2b\sigma_1^2} - \varphi_2 \log \frac{\gamma_2}{\sqrt{2\pi b^2\sigma_2^2}} + \sum_{i=1}^2 \varphi_i \log \varphi_i \right) dx ds$$

Given  $\Theta^0, u^0$ , compute the minimizer of  $\Phi(\Theta, u, \varphi)$  via the following alternating minimization scheme

$$\begin{cases} \varphi^{v+1} = \arg \min_{\varphi \in \Delta} \Phi(\Theta^v, u^v, \varphi) \\ (\Theta^{v+1}, u^{v+1}) = \arg \min_{\Theta, u} \Phi(\Theta, u, \varphi^{v+1}) \end{cases} \quad (11)$$

where  $v$  denotes the inner iteration number.

It can be verified that the sequence defined by (11) has the following properties.  $\mathcal{E}(\Theta, u)$  decreases with respect to  $v$ , that is,

$$\mathcal{E}(\Theta^{v+1}, u^{v+1}) \leq \mathcal{E}(\Theta^v, u^v).$$

Moreover,  $\mathcal{E}(\Theta, u)$  and  $\Phi(\Theta, u, \varphi)$  possess a same global minimizer of  $\Theta$ .

In our context, the original image is always piecewise smooth, we then define a weighted regularizer in the form of

$$R(\nabla u, \nabla^2 u) = \int_{\Omega} (w(x)|\nabla u| + (1-w(x))|\nabla^2 u|) dx, \quad (12)$$

$w(x)$  is a weighting function based on edge detection

Combining (12) with  $\Phi(\Theta, u, \Psi)$  in (11), denoted by  $\Psi(\Theta, u, \varphi^{v+1})$ , we obtain an alternating minimization model (BiLGM-TVBH) for image reconstruction and bias field correction, i.e.,

$$\begin{cases} \varphi^{v+1} = \arg \min_{\varphi \in \Delta} \Psi(\Theta^v, u^v, \varphi) \\ (\Theta^{v+1}, u^{v+1}) = \arg \min_{\Theta, u} \Psi(\Theta, u, \varphi^{v+1}) \end{cases} \quad (13)$$

### III. ALGORITHM AND NUMERICAL EXPERIMENTS

The algorithm of our proposed alternating minimization model is based on the variable splitting technique and the alternating direction method of multipliers (e.g., [16][17]). The minimization problem for  $(\Theta, u)$  can be further separated into two stages, that is, parameters and bias field estimation and image reconstruction.

By introducing auxiliary variables, the proposed unconstrained minimization problem can be reformulated by a constrained sequence of convex optimization subproblems, which can be solved separately by the augmented Lagran-

gian method with some modification on its penalty parameters. Our main idea of the modification is to employ anisotropic diffusion by introducing some adaptive terms in the equation related with the reconstruction. And then, the corresponding minimization problem of the Lagrangian functional is further divided into several sub-problems, from which the parameters  $\Theta$  and the reconstructed version of  $u$  can be solved iteratively.

By routine computation, we get

$$\varphi_1^{v+1} = \frac{\frac{\gamma_1^v}{z(\sigma_1^2)^v} \exp\left(-\frac{|F^v|}{(\sigma_1^2)^v}\right)}{\frac{\gamma_1^v}{z(\sigma_1^2)^v} \exp\left(-\frac{|F^v|}{(\sigma_1^2)^v}\right) + \frac{\gamma_2^v}{\sqrt{2\pi(\sigma_2^2)^v}} \exp\left(-\frac{|K^v|}{z(\sigma_2^2)^v}\right)}, \quad (14)$$

$$\varphi_2^{v+1} = 1 - \varphi_1^{v+1}. \quad (15)$$

where

$$F^v = f \int_{\Omega} \frac{G_{\sigma}}{b^v} ds - Hu^v,$$

$$K^v = \int_{\Omega} G_{\sigma} |f_{b^v} - Hu^v|^2 ds.$$

For simplicity, we only mention the solution of the subproblem for updating  $b$

$$b^{v+1} = \frac{-A_2^{v+1} + \sqrt{(A_2^{v+1})^2 + 4B_2^{v+1}}}{2}, \quad (16)$$

where

$$A_2^{v+1} = \frac{1}{2} \int_{\Omega} \sum_{i=1}^2 \frac{\varphi_i^{v+1}}{(\sigma_i^2)^v} G_{\sigma} \frac{f^2}{b^v} dx, \quad (17)$$

$$B_2^{v+1} = \frac{1}{2} \int_{\Omega} \sum_{i=1}^2 \frac{\varphi_i^{v+1}}{(\sigma_i^2)^v} G_{\sigma} f^2 dx, \quad (18)$$

Some numerical experiments are performed to validate our proposed model and its algorithm on both bias field correction and image enhancement. Figures 1-4 show the results for bias field correction and detail preserving. We find that our method can also preserve details and no ringing artifacts occur near the edges in the reconstructed MR images.

#### IV. CONCLUSION AND FUTURE WORK

We presented a new higher-order variational model that is supposed to reconstruct images which are corrupted by mixed noises, and adjust the intensity inhomogeneity in the images simultaneously.

The alternating minimization model is solved by an efficient ADMM-based algorithm, which reduces the solution to a sequence of convex optimization subproblems. Numerical experiments demonstrate the effectiveness of the proposed model, especially for images in MR.

The main advantage of our proposed model is that it provides a framework for reconstructing images corrupted by mixed noise and degraded by bias field. This is of importance since in some real applications the physics of image acquisition yields noise distributions are the outcome of several noise sources and bias field correction is also indispensable for the image analysis.

Future work will perform experimental comparison with the variational models on the same objective. Furthermore,

the possibility to extend the proposed model to deal with Poisson noise and to color images will be considered.

#### REFERENCES

- [1] N. Pichoff, "The new bound of flash radiography," CLEFS CEA, vol. 54, pp. 58-66, 2006.
- [2] U. Vovk, F. Pernuv, and B. Likar, "A review of methods for correction of intensity inhomogeneity in MRI," IEEE Trans. Med. Imaging, vol. 26(3), pp. 405-421, 2007.
- [3] J. Liu, X.-C. Tai, H.-Y. Huang, and Z.-D. Huan, "A weighted dictionary learning model for denoising images corrupted by mixed noise," IEEE Trans Image Processing, 2013, vol. 22(3), pp. 1108-1120.
- [4] J. Delon and A. Desolneux, "A patch-based approach for removing impulse or mixed Gaussian-impulse noise," SIAM J. Imaging Sciences, 2013, vol. 6(2), pp. 1140-1174.
- [5] M. Hintermüller and A. Langer, "Subspace correction methods for a class of nonsmooth and nonadditive convex variational problems with mixed  $L^1/L^2$  data fidelity in image processing," SIAM J. Imaging Sci., vol. 6(4), pp. 2134-2173, 2013.
- [6] K. Papafitsoros and C.-B. Schönlieb, "A combined first and second order variational approach for image reconstruction," J. Math. Imaging Vis., vol. 48, pp. 308-338, 2014.
- [7] J. Liu, H.-Y. Huang, Z.-D. Huan, and H.-L. Zhang, "Adaptive variational method for restoring color images with high density impulse noise," Inter Jour Comput Vis, vol. 90, pp. 131-149, 2010.
- [8] Z. Gong, Z. Shen, and K. C. Toh, "Image restoration with mixed or unknown," Multiscale Model. Simul., 2014, vol. 12(2), pp. 458-487.
- [9] L. Calatroni, J. De Los Reyes, and C.-B. Schönlieb, "Infimal convolution of data discrepancies for mixed noise removal," SIAM J. Imaging Sciences, vol. 10(3), pp. 1196-1223, 2017.
- [10] G. Steidl, "Combined first and second order variational approaches for image processing," Jahresber Dtsch Math-Ver, vol. 117, pp. 133-160, 2015.
- [11] R. H. Chan, H. Liang, S. H. Wei, M. Nikolova, and X.-C. Tai, "High-order total variation regularization approach for axially symmetric object tomography from a single radiograph," Inverse Problems Imaging, vol. 9(1), pp. 55-77, 2015.
- [12] R. Abraham, M. Bergounioux, and E. Trélat, "A penalization approach for tomographic reconstruction of binary axially symmetric objects," Appl. Math. Optim., vol. 58, pp. 345-371, 2008.
- [13] J. Liu and H.-L. Zhang, "Image segmentation using a local GMM in a variational framework," J. Math. Imaging Vis., vol. 46, pp. 161-176, 2013.
- [14] J. Idier, Bayesian approach to inverse problems. Wiley, New York, 2008.
- [15] A. M. Stuart, "Inverse Problems: A Bayesian Perspectives," Acta Numer., vol. 12, pp. 451-550, 2010.
- [16] V. P. Gopi, P. Palanisamy P, K. A. Wahid, P. Babyn, and D. Cooper "Micro-CT image reconstruction based on alternating direction augmented Lagrangian method and total variation," Comput. Medical Imaging Graph., 2013, vol. 37, pp. 419-429
- [17] R. H. Chan, H. Liang, S. Wei, M. Nikolova, and X.C. Tai, "High-order total variation regularization approach for axially symmetric object tomography from a single radiograph," Inverse Problems & Imaging, 2015, Vol. 9(1), pp. 55-77.

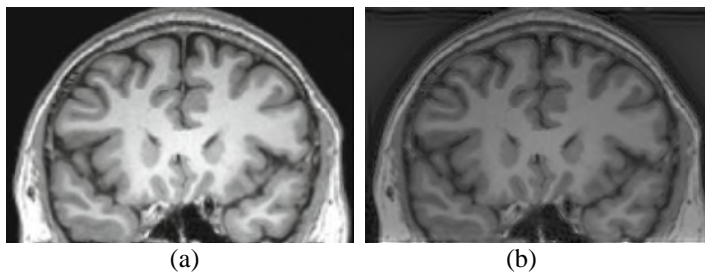


Figure 1. Numerical experiment. (a):Original MRI image, (b): A reconstructed version of (a) obtained by our proposed model.

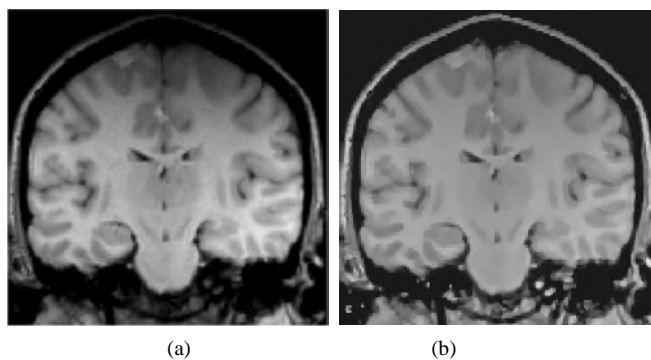


Figure 2. Numerical experiment. (a):Original MRI image, (b): A reconstructed and enhanced version of (a) obtained by our proposed model.

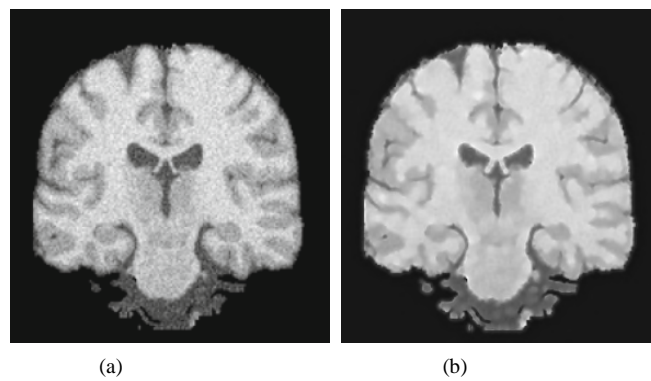


Figure 3. Numerical experiment. (a):Original MRI image, (b):A restored and corrected version of (a) obtained by our proposed model.

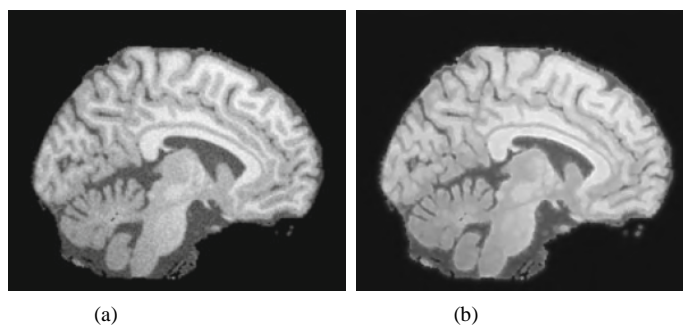


Figure 4. Numerical experiment. (a):Original MRI image, (b):An enhanced version of (a) obtained by our proposed model.

# Irrigation Reservoir Modeling in Catchments without Measurements of Stream Flow

Milan Cisty, Veronika Soldanova, Barbora Povazanova  
 Department of Land and Water Resources Management  
 Slovak University of Technology  
 Bratislava, Slovakia  
 e-mail: milan.cisty@stuba.sk

**Abstract**— This paper considers the determination of time series of river flows in catchments without direct monitoring of this variable. This paper proposes a method for the acquisition of monthly data, which is useful for various purposes. Different parameters of various water management structures can be determined based on information from such data series, such as irrigation reservoir volumes or water demand for irrigation. While identifying unknown stream flows required for such a calculation, authors suppose that historical climatic data for the given area and flows in nearby river catchments are available. This article includes a description of the method of selecting river catchments such that their measured flows can be used in the calculation of an unknown flow of a different stream. This study compares hydrological modeling, linear regression with regularization, and machine learning methods (support vector machines, random forest). Statistical indicators evaluate the calculated flows with the result that the most suitable approach is the support vector machines method using a linear kernel and LASSO regularisation.

**Keywords**-stream flow; ungaged catchment; hydrologic modeling; LASSO; machine learning.

## I. INTRODUCTION

Accurate modeling of flows at watersheds provides the information required to make optimal decisions and inform the optimal design of water management structures. For some purposes (e.g., flood protection), daily or hourly time series of flows are required, but this paper considers the acquisition of monthly data, which is sufficient for various purposes. Different parameters of various water management structures can be determined on the basis of information from such data series, such as irrigation reservoir volumes or water demand for irrigation. This paper considers a typical application requiring such monthly flow series, namely design of an irrigation reservoir.

Irrigation reservoirs are used to retain water during periods of surplus and to control its subsequent use for irrigation in drought periods. In moderately dry regions, such reservoirs are often used to address water management problems in small river catchments, or in marginal parts of larger river catchments. In such places, the irrigation area does not normally exceed a few hundred hectares. These smaller reservoirs are mostly formed by a front dam with a height of 5–12 m, with a volume not exceeding one million m<sup>3</sup> and a surface area of 2–70 ha. In addition to the irrigation function, they also ensure a minimum flow in the stream under the dam, protection against floods, and the creation of conditions for

aquaculture. Smaller streams supply such reservoirs at the margins of river catchments. Such smaller streams often do not have systematic measurements of their flow, and therefore determination of this quantity is the subject of this paper.

In designing a reservoir, it is important to evaluate its function and assess its water management, e.g., its ability to provide the required amount of water for irrigation. The assessment of small water reservoirs represents a set of tasks dealing with the evaluation of the reservoir from the point of view of the quantitative balance of water. For irrigation reservoirs, this is mostly the seasonal, annual, rarely multi-year management of outflow and storage. The water management considerations include the management of the supply volume for securing of required functions (irrigation, recreation, fish breeding), managing the protection function of the reservoir volume (flood protection), and determining the requirements for the outflow, abstraction of water, and other parameters.

The input data used in the water management calculation of reservoirs include the water inflow into the reservoir, demand for water abstraction from the reservoir, data on compulsory outflow of water below the reservoir, and the evaporation and other losses of water from the reservoir. Such data are required retrospectively every month for at least 30 years. Such a long period should include sufficient occurrence of dry and wet years needed for the objective calculations. As stated, data on inflow are often unavailable, as there are rarely long-term measurements of the catchments with a small area.

The contribution of this article is a comparison of the various methods for determining river flows for the calculations needed when designing a small water reservoir. The authors are not aware of the previous works directly aimed at this topic, although, part of this task - flows determination in watersheds without measurements alone, was studied by various authors. A survey of regional methods used in Slovakia, from where the case study presented later in this paper is located, was reported by [1]. A good introduction to the topic is given by [2]. The determination of unmeasured flows can be conducted using hydrological models [3], regression methods [4], or artificial neural networks [5].

In this paper, several methods of undertaking the given task are compared. The objective is to acquire the monthly flows required for the balance calculation verifying the supply function of the irrigation reservoir. In Section II, the acquisition and preparation of the data are described. The methods applied in this study are briefly explained in Section III. In Section IV, the settings of the experimental

computations are described, and the results are evaluated and discussed. Finally, Section V summarizes the main findings of this study.

## II. CASE STUDY AND DATA DESCRIPTION

This paper reports a case study of the Parna stream, which is a small mountain stream in the Small Carpathians in Western Slovakia. Its catchment area is 45.59 km<sup>2</sup>. To determine the average daily flow in this stream, known flow data from similar nearby catchments are used (Figure 1).

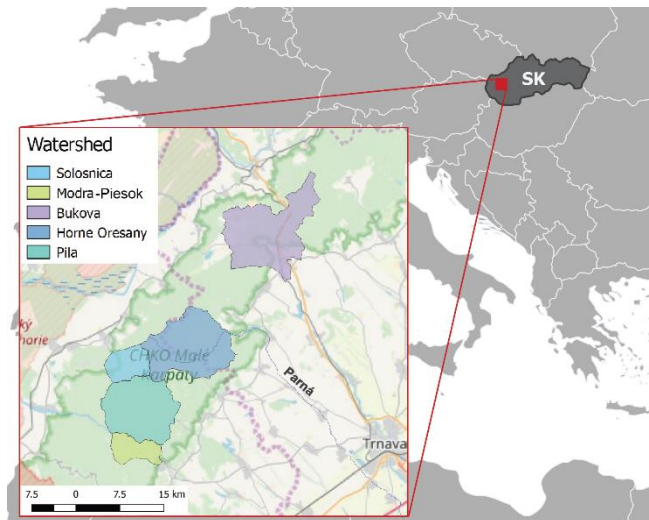


Figure 1. Situation of selected water catchments. © OpenStreetMap contributors (partly)

Data from water metering stations at Bukova (catchment of Trnavka), Modra (catchment of Vistucky stream), Pila (catchment of Gidra), and Solosnica (Solosnický stream catchment) were used. The daily flow data for the river catchments were obtained from the Slovak Hydrometeorological Institute in Bratislava, Slovakia. Climatic data from the European Climate Assessment & Dataset (ECA&D) were also used in this study. ECA&D is composed of 69 participating organizations from 63 countries. The network of basic metering stations from which the data are derived covers the European and Mediterranean regions. It records 12 climatic elements. The main product of this initiative (E-OBS), which was used in this work, is a daily gridded observational dataset for precipitation, temperature, and sea level pressure for Europe. The climatic data in ECA&D are provided as a spatial time series in the netCDF format for the period 1950–2018, cover a spatial scope of 25°N–75°N and 40°E–75°E, and have a spatial resolution of 0.25°×0.25°. Data from 1 January 1980 to 31 August 2017 were used. Time series of the daily values of potential evapotranspiration in individual water catchments were calculated using the climatic data. The potential evapotranspiration was calculated using a formula proposed by Oudin in [6]. The advantage of Oudin's formula is that it only requires the minimum and maximum temperatures as inputs. As stated in this paper, this simplification of the inputs

does not significantly affect the precision of the flow modeling in hydrological models.

## III. METHODS

The main objective of this paper is to reassess the water management function of small water reservoirs built in the past. Since they were built, the climate conditions have changed, and the demand for irrigation water is likely to have increased. The operating volume of reservoirs is often reduced from its original design value by years of sedimentation. As stated, the limiting factor in these calculations is the fact that the inflow into the reservoirs is, in many cases, not measured, i.e., it cannot be applied in the water balance calculation of the reservoir. The cause of this situation is that small-size streams often lack measurements. In this paper, regression methods and hydrological modeling are compared for determination of such unknown historical flows. To evaluate the performance of these methods, the case study for Horne Oresany reservoir on Parna stream was performed, e.g., in water catchment where the flows are known. The results of the computation methods were evaluated by suitable statistical indicators and by a comparison of the results of the reservoir water balance using either measured or simulated flows. A brief characterisation of these methods is given below.

The most common regression method is Multiple Linear Regression (MLR). MLR analysis is generally used to find the relevant coefficients in the following equation using the least-squares method. The basic equation is:

$$Y = \beta_0 + \beta_1 * X_1 + \beta_2 * X_2 + \beta_3 * X_3 + \dots + \epsilon, \quad (1)$$

where  $Y$  is the dependent variable,  $X_i$  are explanatory variables,  $\beta_0$  is the intercept (constant term),  $\beta_i$  is the slope coefficient for each explanatory variable, and  $\epsilon$  is the model error term.

A major condition for linear regression is that the explanatory variables  $X_i$  must be relatively uncorrelated. However, some correlation is likely to occur in the task addressed in this study. More suitable algorithms than basic linear regression were therefore used. Least Absolute Shrinkage and Selection Operator (LASSO) applied in this paper redefine linear regression to prevent the effect of multicollinearity and help ensure a more stable model by penalizing and subsequently reducing the number of MLR coefficients [7].

A Support Vector Machine (SVM) is a supervised machine learning method that can be used to calculate regression tasks. Its characteristic feature is the kernel trick—a nonlinear mapping that transforms the original training data of a non-linear problem (which is the case in our scenario) into a higher-dimensional form [8]. Another important concept of the SVM methodology is its ability to ignore small errors. As a consequence, the SVM model has good generalization abilities.

Random Forests (RF) [9] are formed by a set of trees, which can either be classification or regression trees, depending on the problem being addressed. An RF prediction is an average of many trees (weak learners) grown on a bootstrap sample of the training data. The user chooses the

number of trees in the forest (ensemble). Each tree is trained using a different bootstrap sample, which causes that different trees are obtained. For the regression task, the values predicted by each tree are averaged to get the final random forest prediction.

Next method used for the calculation of unknown flows is the TUV hydrological model [10]. This model runs on a daily time step and consists of a snow routine, a soil moisture routine, and a flow routing routine. The snow routine simulates snow accumulation and melting using a degree-day concept. The soil moisture routine simulates runoff generation and changes in the soil moisture state of a catchment. Upper and lower soil reservoirs represent runoff routing. A genetic algorithm was used to calibrate the 15 parameters of this conceptual model.

The following formula generally defines the relationship between the inflow of water to the reservoir and outflow of water from the reservoir:

$$\Delta V = (I - O) \Delta t, \tag{2}$$

where  $\Delta V$  expresses the change in volume of water in the reservoir over time,  $I$  is the inflow to the reservoir,  $O$  denotes the outputs (outflow, water extraction, and losses), and  $\Delta t$  is the time step for the evaluation of the balance.

For this study, to implement the water balance in the reservoir, a computer program was set up in R [11] to model the accumulation of water in the reservoir. The basic objective is to reassess the feasibility of the requested water extraction from the reservoir. The model operates on a monthly time step. Different time step (e.g., two weeks) is also possible, but not necessary for this task, as experiences from building and managing irrigation reservoirs confirms (e.g., flood protection function of a reservoir, where a much smaller time step is required is an entirely different task than that, being solved herein). It is also necessary to note that the use of the previous period, when designing a new reservoir already defines a level

of accuracy which will not be significantly improved by a more detailed time step. The hydrological data used in the model are also specified in monthly values.

#### IV. RESULTS AND DISCUSSION

To determine the unknown flows required for the water balance model of the irrigation reservoir, the following steps were evaluated:

1. Analysis of the river catchment above the reservoir, in which the absence of flow measurements is assumed (Velke Oresany catchment, Parna stream), and selection of suitable river basins for their calculation using the hydrological analogy method.
2. Analogous calculation of unknown flows using hydrological modeling.
3. Analogous calculation of unknown flows using statistical and machine learning methods.
4. Calculation of water management balance of the reservoir with measured flows (used only in the context of testing) and with simulated flows acquired by various methods.
5. Evaluation and comparison of results.

##### A. Selection of Suitable River Catchments

The outflow regime of the river catchment depends on its climate conditions, on topographic features, geological conditions, types of prevailing soils in the river basin, land use of the area, etc. The river basins for the analogous calculation should be similar to the river catchment where the flow is to be determined. Moreover, it is advantageous to select analogous river catchments as close as possible to the catchment of interest, as some climate, topological, geological, and other properties change relatively smoothly, so nearby river catchments could have many similar features, and consequently can have a similar genesis of the outflow (Figure 1).

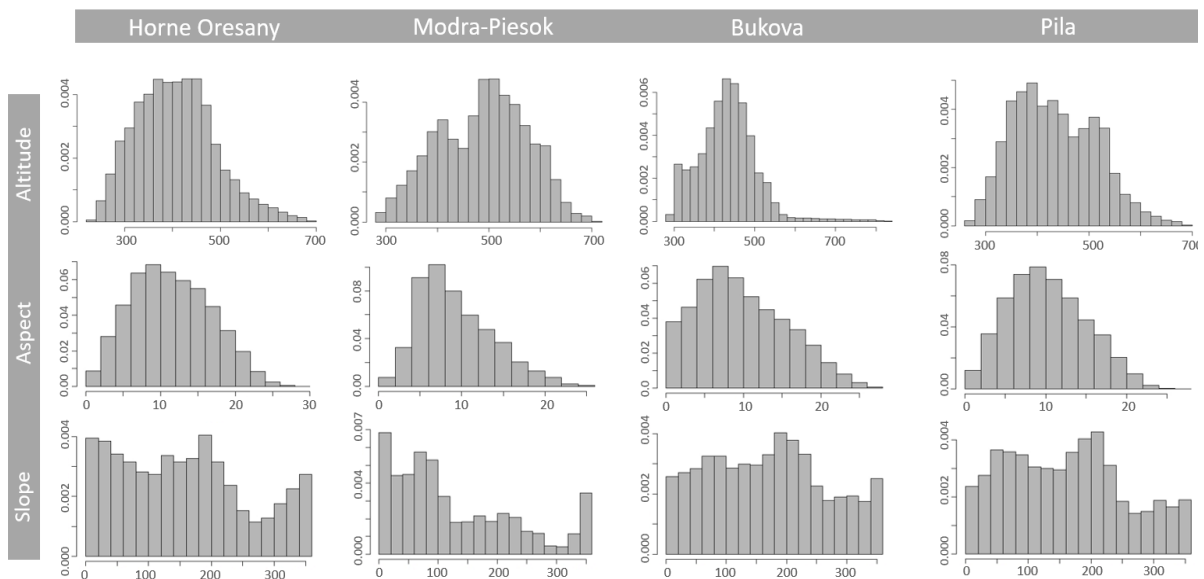


Figure 2 Histograms of altitudes [m a.s.l.], aspect [° north] and slope [° horizontal] of river catchments.

Several analyses were elaborated for this purpose; Selected parts of this analysis are shown in Figure 2 and described in Table I.

Figure 2 shows the analyses of the topography (altitudes, aspect, slope), as the nature of landscape cover, weather, and the amount and type of rainfall change with these properties. Such phenomena will impact water outflow from the river catchment (as will, for example, the winter flow regime). The river catchments used in this study are located at altitudes of approximately 300–700 m above sea level. This histogram representation of altitudes allows a visual assessment of the similarity of river catchments. The most similar catchment to the Horne Oresany catchment, where we want to determine the flows is the Pila basin in all the features shown (altitude, slope, aspect).

The representative part of the analyses is evaluated in Table I. This table and GIS analyses show that, for the assessed river catchments and from the point of view of catchment features influencing the outflow regime, the Parna river catchment is most similar to the Gidra catchment (Pila gauging station) and the Vistucky stream catchment (Modra-Piesok station). Similarity can be seen in numerical evaluation of basic topographic characteristics, percentage of soil types and land use. Different soil types vary in terms of the ratio of infiltration and the outflow of water during periods of rain, in the ability to retain water in the soil, and in other properties that influence the outflow of water from the river catchment. Similarly, land use (for example, a forest versus arable land) also has a significant impact on river basin drainage properties. These two catchments will be therefore preferred in the following calculations. Also other analyses were accomplished, but cannot be described in more detail here for reasons of brevity.

**B. Hydrological Modeling**

The unknown flows were calculated by the TUV conceptual rainfall-runoff model, with a genetic algorithm used for calibration. The calculation was performed in daily step, and the daily flows were subsequently converted into

monthly flows. The calibration was implemented based on flow and climate data from the Pila catchment which, based on previous analysis, was assessed as being the most similar to the river catchment in which the unknown flows were to be calculated. The optimum parameter values of the TUV model were acquired by the genetic algorithm using the flow and climate data from the Pila catchment. These parameters were subsequently applied in the modeling of the river catchment with the unknown flows (Velke Oresany–Parna) using the local climate data. The genetic algorithm population was set to 500, the number of parameters to be determined was 15, and the maximum number of generations was 20. The objective function sought to minimise the Mean Absolute Scaled Error (MASE), a statistical variable suggested by Hyndman [12]. This statistic is preferable to the Nash–Sutcliffe Efficiency [13] in this case, as the final objective is to calculate monthly flows. This is because the MASE does not take into consideration the power of flows, and thus does not emphasize the calculation of large daily values, which are not herein priorities because of the transformation (averaging) of calculated daily values into monthly values. The calculated daily and monthly inflows to the Horne Oresany reservoir are compared with the measured values in Table II.

**C. Regression Calculation**

To calculate the flows at the Horne Oresany river reservoir on the Parna stream, regression methods were also applied. These computations used the assumption that flow measurements had recently started in the Parna river catchment as a requirement for the determination of longer series of historical flows. The measurements were assumed to have started at the beginning of 2016 (whole period is 1980–2017). The regression relations were then derived based on this period and applied for the whole historical period of interest.

TABLE I. COMPARISON OF RIVER CATCHMENT FEATURES

Watershed	Area (ha)	Surface Characteristics (median)			Soil Types (%)			Land Use (%)				
		Elevation (m a.s.l.)	Slope (°)	Aspect (°)	Loamy	Loamy-sand	Sandy-loam	Arable land	Broad-leaved forest	Mixed forest	Transitional woodland/shrub	Urban fabric
<b>Bukova</b>	4296.1	332.4	9.0	170	82.5	0	17.5	23.9	60.7	6.9	2.1	4.9
<b>Modra-Piesok</b>	937.7	495.1	8.0	92.9	0	54.3	45.7	0	91.5	0	8.5	0
<b>Horne Oresany</b>	3733.1	403.1	11.1	151	38	0	62	0	90.9	0.8	8.2	0
<b>Pila</b>	3289.9	426.7	9.8	161	12.8	16.3	70.9	0	92.4	0	7.1	0.5
<b>Solosnica</b>	1046.5	420.8	16.3	195	100	0	0	0	94.4	0	5.6	0

Methods described in the previous subsections were used for the regression calculation. A grid search combined with a repeated cross-validation methodology was used to find the parameters of these models. In this approach, a set of model parameters from a predetermined grid is sent to the evaluating algorithm. A set of parameters was sent to the repeated cross-validation mechanism, which is used for the evaluation of the parameter combinations [14]. The calculation was performed in R language [11].

The unknown flows in the Parna stream were calculated using flows from four “analogous” river catchments and from the average daily temperature, rainfall, and potential evapotranspiration in the Parna river catchment. As the flow from a catchment is influenced not only by the current values of climate variables, but also by their values from previous days, climate data from seven days before the date of the prediction were also included. As the longer history of hydro-climatic developments in the catchment must also be described in the input data, three variables summarizing the previous precipitation (cumRAIN7, cumRAIN14, cumRAIN21) and variables summarizing the previous evapotranspiration (cumPET7, cumPET14, cumPET21) were constructed. (The numbers in these variable names denote how many days they are summarising.) In this way, a training set with 35 explanatory variables was created. This set covers the period of anticipated short-term measurements on the Parna stream for 608 days (only data up to August were available for 2017). The test file includes the same variables, but the data relate to the whole period 1980–2017, i.e., it contains 13,738 lines (one per day).

TABLE II. EVALUATION OF MODELS

Statistic	TUW	MLR	LASSO	SVM	RF
RMSE	0.41	0.14	0.14	0.14	0.15
NSE	0.65	0.78	0.78	0.78	0.73
r	0.81	0.89	0.89	0.89	0.88
R2	0.66	0.79	0.79	0.79	0.77
VE	0.65	0.72	0.72	0.72	0.70

RMSE – Root Mean Square Error, NSE - Nash-Sutcliffe Efficiency, r - Correlation Coefficient, R2 – Coefficient of Determination, VE - Volumetric Efficiency

The results of the regression calculation are presented in Table II, which indicates that the regression provides relatively balanced results using different statistical and machine learning methods. The best methods are SVM, the regularised linear method using the LASSO-type regularisation, and, surprisingly, the simple MLR. However, the latter method cannot be recommended, as linear regression requires the explanatory variables to be relatively uncorrelated with each other. This multicollinearity principle is violated for this task, and the results using MLR are therefore expected to be unstable; for other streams, they may be less precise than in this case. Relatively poor results are obtained by the random forest technique (RF), which is a popular ensemble tree method. The authors believe that the problem with the random forest method is that it is based on regression trees which have no extrapolation ability. Described regression task used a relatively short training period, and there is a high possibility

that there were no extremes during this period. Thus, the random forest was not able to learn such events. Although this does not influence so much, e.g., the simple linear regression, for RF method it is quite important.

#### D. Water Balance of the Reservoir

The water balance of the reservoir was computed using the measured and calculated inflows to the reservoir to verify whether the precision of the monthly flows computed by various analogy methods is sufficient for this purpose. To calculate the balance, a function was programmed in R to take various input data. The main data are the required time series of monthly irrigation amounts and water inflow to the reservoir from Parna stream. Additionally, these data include the requisite altitudes of the minimum and maximum reservoir levels, the minimum and maximum water volume in the reservoir, the irrigated area, evaporation data from the water surface, and the ecological flow that must be respected below the reservoir. The water body of the reservoir is defined by a curve of water surface areas and water volumes depending on the water level in the reservoir. This curve (or table) can be determined from a topographic survey and is also part of the input data.

The balance of the reservoir was firstly calculated using flows calculated by analogy and then using the measured data. Two methods were used to compare the acquired results. The first was the establishment of the irrigation security, which is the ratio of supplied and required irrigation as a percentage:

$$IrrSecured = (ZSupplied/ZRequired)*100, \quad (3)$$

The correlation among the computed annual amount of irrigation water has been also evaluated on the basis of the computations with measured and calculated flows. The resulting data are summarised in Table III, which demonstrates the suitability of the applied methods. The security of irrigation (availability of water in the reservoir) is also expressed in Figure 3, where a relatively high agreement can be seen as regards the security of irrigation when using the calculated and measured flows.

TABLE III. IRRIGATION SECURITY EVALUATION

Method	Yearly correlation with computed by measured flows	Irrigation security in %
Measured flows	1.00	84.96
TUW	0.90	90.23
MLR	0.90	86.79
LASSO	0.92	87.77
SVM	0.90	87.04
RF	0.89	89.88

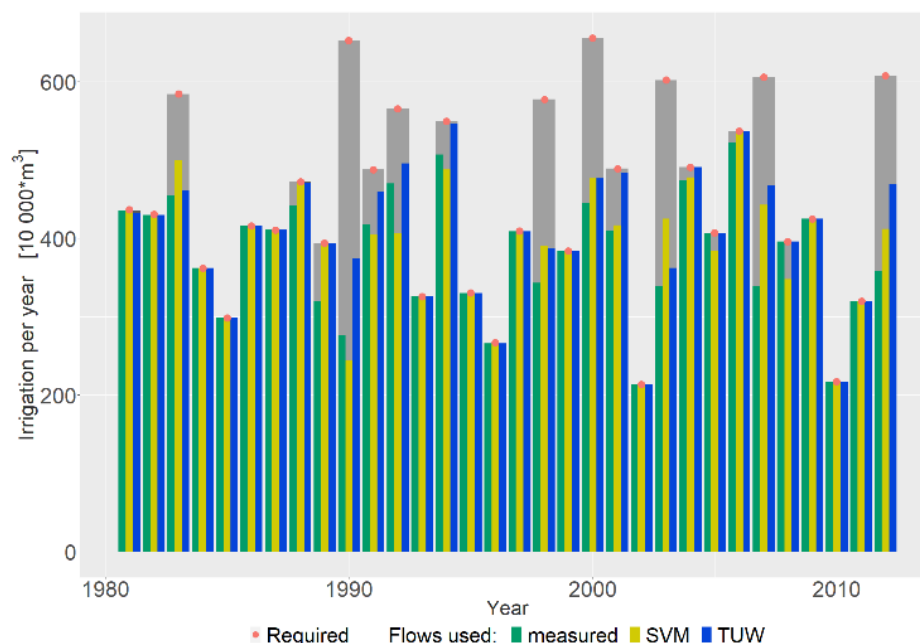


Figure 3. Graphical comparison of security of irrigation.

## V. CONCLUSION

The objective of this study was to compare various methods of calculating unknown flows in the context of engineering computations, such as evaluation of water balance of an irrigation reservoir. The methods compared include regression and hydrological modeling methods. If at least short-term measurements are available for the relevant river catchment, a most suitable method is the flow calculation method using regression with LASSO regularisation, as this eliminates the problem of multicollinearity in the input data. Another suitable method is the machine learning SVM method, which offers good generalisation ability. This is a major advantage for computations on small river catchments (such as that used in this study), where relatively significant uncertainties can be expected as regards data and modeling. If no flow data are available, a hydrological model must be used. In this paper, the use of the TUV model was applied. Computation of flows by TUV model was slightly less precise than by using regression methods, but the subsequent verification of calculated flows using TUV model in the context of an irrigation reservoir balance, also demonstrated its usability in the context of engineering calculations.

## ACKNOWLEDGEMENT

This work was supported by the Slovak Research and Development Agency under Contract No. APVV-15-0489 and by the Scientific Grant Agency of the Ministry of Education of the Slovak Republic and the Slovak Academy of Sciences, Grant No. 1/0662/19.

## REFERENCES

- [1] S. Kohnova, J. Szolgay, L. Solin, and K. Hlavcova, "Regional methods for prediction in ungauged basins," Ostrava: Key Publishing, p. 113, 2006, ISBN: 80-87071-02-6
- [2] M. Hrachowitz et al., "A decade of predictions in ungauged basins (PUB)—a review," *Hydrological sciences journal*, vol. 58(6), pp. 1198-1255, 2013.
- [3] A. Viglione et al., "Comparative assessment of predictions in ungauged basins - Part 3: Runo signatures in Austria," *Hydrology and Earth System Sciences*, vol. 17, pp. 2263-2279, 2013, doi:10.5194/hess-17-2263-2013, 2017
- [4] M. S. Gibbs, H. R. Maier, and G. C. Dandy, "A generic framework for regression regionalization in ungauged catchments," *Environmental modeling & software*, vol. 27, pp. 1-14, 2012.
- [5] V. Kuzmin et al., "Method of prediction of the stream flows in poorly gauged and ungauged basins," *Journal of Ecological Engineering*, vol. 20(1), pp. 180-187, 2019.
- [6] L. Oudin, C. Michel, and F. Anctil, "Which potential evapotranspiration input for a lumped rainfall-runoff model?: Part 1 - Can rainfall-runoff models effectively handle detailed potential evapotranspiration inputs?," *Journal of Hydrology*, vol. 303/ Nos. 1-4, pp. 275-289, 2005.
- [7] J. Friedman, T. Hastie, and R. Tibshirani, "Regularization paths for generalized linear models via coordinate descent," *Journal of Statistical Software*, vol. 33(1), pp. 1-22, 2010.
- [8] V. Vapnik, "The Support vector method," *International Conference on Artificial Neural Networks*, Springer, Berlin, Heidelberg, pp. 261-271, 1997.
- [9] L. Breiman, "Random forests," *Machine Learning*, vol. 45(1), pp. 5-32, 2001.
- [10] A. Viglione and J. Parajka, "TUVmodel: Lumped hydrological model for education purposes," R package

- version 1.0-1., 2018, Available from: <https://CRAN.R-project.org/package=TUWmodel> [retrieved July, 2019]
- [11] R Core Team, "R: A language and environment for statistical computing," R Foundation for Statistical Computing, Vienna, Austria, 2019, Available from: <https://www.R-project.org> [retrieved July, 2019]
- [12] R.J. Hyndman, and G. Athanasopoulos, "Forecasting: principles and practice," OTexts, 2018.
- [13] F. Lin, X. Chen, and H. Yao, "Evaluating the use of Nash-Sutcliffe efficiency coefficient in goodness-of-fit measures for daily runoff simulation with SWAT," Journal of Hydrologic Engineering, vol. 22(11), p.05017023, 2017.
- [14] C. Bergmeir, R.J. Hyndman, and B. Koo, "A note on the validity of cross-validation for evaluating autoregressive time series prediction," Computational Statistics and Data Analysis, 120, pp.70-83, 2018.

# Code Verification of PECM with Strongly Discontinuous Flows

Zhibo Ma

Institute of Applied Physics and Computational Mathematics

Beijing, China

e-mail: mazhibo@iapcm.ac.cn

**Abstract**—The simulation of compressible flows with strong discontinuities is necessary to verify meshfree methods. In order to eliminate inconsistencies between mathematics and physics of existing meshfree methods exposed especially when discontinuities exist, a different set of kernel functions, modularizing factors and discrete equations is put forward by a new meshfree method named Physics Evoked Cloud Method (PECM). In this paper, PECM is briefly introduced and is verified by posteriori assessments based on comparisons between numerical and exact solutions. The assessments show that PECM has overcome shortcomings of existing meshfree methods and is able to accommodate various kinds of strong discontinuities including large density ratio, from which we see that PECM has an excellent robustness and a high accuracy.

**Keywords**—PECM; RKPM; meshfree method; code verification.

## I. INTRODUCTION

The ability and accuracy of numerical computation are the most important credibility indices for modeling and simulations [1][2]. For discontinuous problems such as shock waves or contact between different materials, spatial derivatives of pressure, density, and velocity etc. may not exist. Consequently the numerical methods are usually constructed according to the ideas put forwarded by Von Neumann or Godunov [3][4]. Neumann method captures physical discontinuities by adding artificial viscosity terms, whereas Godunov method does that by Riemann solutions. In this paper, we call the artificial terms modularizing factors in simulations, as they represent the microscopic phenomena through physical quantities corresponding to macroscopic discrete bodies and time steps.

As a purely Lagrangian meshfree method, Smoothed Particle Hydrodynamics (SPH) based on Neumann idea has undergone a long-term development and has earned very wide attentions [5][6]. Since it was put forward in 1977, efforts have been made to improve its accuracy, therefrom some derivative methods of SPH were proposed, such as Reproducing Kernel Particle Method (RKPM), Corrective Smoothed Particle Method (CSPM) and Modified Smoothed Particle Hydrodynamics (MSPH) [7]-[9]. Unfortunately, SPH and its derivative methods narrated above still display obvious shortcomings especially when they are applied in dynamic problems where strong discontinuities exist.

According to the idea of Taylor's series expansion, an arbitrary function can be approximated by polynomials. As the polynomial and its derivative are easily to be constructed, correction functions formed as polynomial have been generally used to modify the kernel functions of SPH. All the derivative methods including RKPM, CSPM, and MSPH use

this mechanism to improve the accuracy of kernel estimation. However, these improvements originated just from mathematical ideas, so the physics laws have not been fully reflected by the numerical algorithms. For problems such as explosions or impacts with multi-materials, in which many kinds of discontinuity exist, these improvements are not remarkable, and the meshfree simulations are still difficult to avoid the large uncertainties, numerical oscillations or even nonphysics solutions.

In order to eliminate the deficiencies firmly tangled in the existing meshfree methods and greatly enhance the adaptability of numerical method, the author of this paper proposed a new method named Physics Evoked Cloud Method (PECM) and developed a software named How Are Universes Cuddling (HAUC) based on PECM [10]-[14]. In fact, PECM is a meshfree hierarchical methodology built according to the classification of multifarious materials. PECM has no specific restriction on the approach of meshfree approximation but six principles should be generally satisfied, one of which says that PECM should correctly reflect objective physics laws. At present, PECM temporarily use the approach of kernel approximation but the numerical algorithms were rearranged deeply in order to satisfy its general principles.

In this paper, RKPM is selected as a representative of SPH and its derivative methods. Preceding with description of governing equations and time stepping scheme in section II, RKPM and PECM for fluid dynamics are briefly described in section III and section IV. Section V addresses code verification aims to assess the credibility of PECM by a posteriori approach. Section VI gives conclusions and the article is closed with an acknowledgement. All the numerical and exact results were produced by HAUC.

## II. GOVERNING EQUATIONS AND TIME STEPPING SCHEME FOR SIMULATIONS

For fluid flows without external force, heat conduction and physics viscosity, the Lagrangian forms of differential governing equations are:

$$\text{Mass} \quad \frac{d\rho}{dt} = -\rho \nabla \cdot \mathbf{v} \quad (1)$$

$$\text{Momentum} \quad \frac{d\mathbf{v}}{dt} = -\frac{1}{\rho} \nabla p \quad (2)$$

$$\text{Energy} \quad \frac{de}{dt} = -\frac{p}{\rho} \nabla \cdot \mathbf{v} \quad (3)$$

Where  $\rho$ ,  $\mathbf{v}$ ,  $p$ ,  $e$  and  $t$  indicate density, velocity, pressure, internal energy and time, respectively.

During the time stepping as solving the unsteady flows corresponding (1) – (3), a two-step scheme consists of prediction and correction is adopted as in (4) – (5).

$$\text{Prediction: } \psi^{n+\frac{1}{2}} = \psi^n + 0.5\Delta t(d\psi/dt)^n \quad (4)$$

$$\text{Correction: } \psi^{n+1} = \psi^n + \Delta t(d\psi/dt)^{n+\frac{1}{2}} \quad (5)$$

Where  $\psi$  generally refers to  $\rho, e, \mathbf{v}, \mathbf{r}, h$ , and  $\mathbf{r}$  is the position coordinates of discrete body,  $h$  is smoothing length for kernel approximation. By sound speed  $c$  and a factor  $\tau$  related to CFL conditions, we have time step  $\Delta t = \tau h / (c + |\mathbf{v}|)$ , and  $p$  is obtained via equation of state  $p = p(\rho, e)$  in each time step.

In this paper, the numerical simulations with RKPM or PECM are all based on the governing equations and time stepping scheme narrated above.

### III. DESCRIPTION OF RKPM

The ideas and schemes of RKPM are as follows.

#### A. Kernel Estimation

Kernel estimation of SPH for an arbitrary function  $f(\mathbf{r})$  can be described as

$$\langle f(\mathbf{r}) \rangle = \int_{\Omega} f(\mathbf{r}') W^{(\text{SPH})}(\mathbf{r} - \mathbf{r}', h) d\mathbf{r}' \quad (6)$$

Where  $W^{(\text{SPH})}(\mathbf{r} - \mathbf{r}', h)$  is a compact kernel function with its support domain  $\Omega$  and smoothing length  $h$ .  $\mathbf{r}'$  and  $d\mathbf{r}'$  are respectively, the coordinates and volume of discretized micro-bodies, which is centered by coordinates  $\mathbf{r}$  in  $\Omega$ . With integration by part and Gaussian formula, estimations of derivatives can be shifted to the kernel function, such as

$$\langle \nabla f(\mathbf{r}) \rangle = \int_{\Omega} f(\mathbf{r}') \nabla_r W^{(\text{SPH})}(\mathbf{r} - \mathbf{r}', h) d\mathbf{r}' \quad (7)$$

Where the operator  $\nabla_r$  represents the derivation with  $\mathbf{r}$ . RKPM has inherited all the SPH algorithms except the kernel function, which is corrected as

$$W^{(\text{RKPM})}(\mathbf{r} - \mathbf{r}', h) = C^{(\text{RKPM})}(\mathbf{r} - \mathbf{r}', h) W^{(\text{SPH})}(\mathbf{r} - \mathbf{r}', h) \quad (8)$$

Briefly noting  $\mathbf{r}_{ij} = \mathbf{r}_i - \mathbf{r}_j$  and  $b_j$  the volume of particle  $j$ , the  $n_c$ -order correction  $C_{ij}^{(\text{RKPM})} = C^{(\text{RKPM})}(\mathbf{r}_{ij}, h_i)$  in form of polynomial is solved by the consistency conditions as

$$\sum_{j=1}^N b_j C_{ij}^{(\text{RKPM})} W_{ij}^{(\text{SPH})} = 1 \quad (9)$$

$$\sum_{j=1}^N b_j C_{ij}^{(\text{RKPM})} W_{ij}^{(\text{SPH})} \mathbf{r}_{ij}^k = 0, \quad k = 1, 2, \dots, n_c \quad (10)$$

#### B. Modularizing Factors

Modularizing factors of RKPM are the same of those in SPH, such as artificial pressure

$$\Pi_{ij}^{(\text{SPH})} = \begin{cases} (-\alpha c_{ij} \mu_{ij} + \beta \mu_{ij}^2) / \rho_{ij} & \mathbf{v}_{ij} \cdot \mathbf{r}_{ij} < 0 \\ 0 & \mathbf{v}_{ij} \cdot \mathbf{r}_{ij} \geq 0 \end{cases} \quad (11)$$

And artificial heat flux is

$$\mathbf{H}_{ij}^{(\text{SPH})} = \begin{cases} 2\zeta_{ij}(\mathbf{e}_i - \mathbf{e}_j)\mathbf{r}_{ij} & \mathbf{v}_{ij} \cdot \mathbf{r}_{ij} < 0 \\ \rho_{ij}(\mathbf{r}_{ij}^2 + \eta h_{ij}^2) & \mathbf{v}_{ij} \cdot \mathbf{r}_{ij} \geq 0 \end{cases} \quad (12)$$

Where particle  $j$  is in the support domain  $\Omega_i$  of particle  $i$ , and  $\mathbf{v}_{ij} = \mathbf{v}_i - \mathbf{v}_j$ ,  $h_{ij} = (h_i + h_j)/2$ ,  $c_{ij} = (c_i + c_j)/2$ ,  $\rho_{ij} = (\rho_i + \rho_j)/2$ ,  $\mu_{ij} = h_j \mathbf{v}_{ij} \cdot \mathbf{r}_{ij} / (\mathbf{r}_{ij}^2 + \theta h_{ij}^2)$ ,  $\zeta_{ij} = (\zeta_i + \zeta_j)/2$ ,  $\zeta = g_1 h c + g_2 h^2 (|\nabla \cdot \mathbf{v}| - \nabla \cdot \mathbf{v})$ ,  $\alpha, \beta, \varepsilon, \eta, g_1, g_2$  are constants.

#### C. Discrete Equations

The standard discrete equations of RKPM for mass, momentum and energy, are written in (13) – (15).

$$\frac{d\rho_i}{dt} = \sum_{j=1}^N m_j \mathbf{v}_{ij} \cdot \nabla_i W_{ij}^{(\text{RKPM})} \quad (13)$$

$$\frac{d\mathbf{v}_i}{dt} = - \sum_{j=1}^N m_j \left( \frac{p_i}{\rho_i^2} + \frac{p_j}{\rho_j^2} + \Pi_{ij}^{(\text{SPH})} \right) \nabla_i W_{ij}^{(\text{RKPM})} \quad (14)$$

$$\frac{de_i}{dt} = \frac{1}{2} \sum_{j=1}^N m_j \left[ \left( \frac{p_i}{\rho_i^2} + \frac{p_j}{\rho_j^2} + \Pi_{ij}^{(\text{SPH})} \right) \mathbf{v}_{ij} + \mathbf{H}_{ij}^{(\text{SPH})} \right] \cdot \nabla_i W_{ij}^{(\text{RKPM})} \quad (15)$$

Where  $W_{ij}^{(\text{RKPM})} = W^{(\text{RKPM})}(\mathbf{r}_{ij}, h_i)$ ,  $N$  is the total particle number in  $\Omega_i$ , the operator  $\nabla_i$  means the derivation with  $\mathbf{r}_i$ .

### IV. DESCRIPTION OF PECM

The ideas and schemes of PECM are as follows.

#### A. Kernel Estimation

PECM calls the micro-body as cloud other than particle in SPH, and uses a new kernel for momentum equation as

$$W^{(\text{PECM})}(\mathbf{r} - \mathbf{r}', h) = C^{(\text{PECM})}(\mathbf{r} - \mathbf{r}', h) W^{(\text{SPH})}(\mathbf{r} - \mathbf{r}', h) \quad (16)$$

The correction  $C_{ij}^{(\text{PECM})}$  observes new consistencies

$$\sum_{j=1}^N b_j \rho_j C_{ij}^{(\text{PECM})} W_{ij}^{(\text{SPH})} = 1 \quad (17)$$

$$\sum_{j=1}^N b_j \rho_j C_{ij}^{(\text{PECM})} W_{ij}^{(\text{SPH})} \mathbf{r}_{ij}^k = 0, \quad k = 1, 2, \dots, n_c \quad (18)$$

#### B. Modularizing Factors

PECM has two pressure factors as

$$\Pi_{ij,1}^{(\text{PECM})} = \begin{cases} (-\alpha c_{ij} \mu_{ij} + \beta \mu_{ij}^2) \rho_{ij} & \mathbf{v}_{ij} \cdot \mathbf{r}_{ij} < 0 \\ 0 & \mathbf{v}_{ij} \cdot \mathbf{r}_{ij} \geq 0 \end{cases} \quad (19)$$

$$\Pi_{ij,2}^{(\text{PECM})} = \begin{cases} (-\alpha c_{ij} \mu_{ij} + \beta \mu_{ij}^2) \hat{\rho}_{ij} & \mathbf{v}_{ij} \cdot \mathbf{r}_{ij} < 0 \\ 0 & \mathbf{v}_{ij} \cdot \mathbf{r}_{ij} \geq 0 \end{cases} \quad (20)$$

The heat flux factor is modified as

$$\mathbf{H}_{ij}^{(\text{PECM})} = \begin{cases} \zeta_{ij} \rho_{ij} (\mathbf{e}_i - \mathbf{e}_j) \mathbf{r}_{ij} & \mathbf{v}_{ij} \cdot \mathbf{r}_{ij} < 0 \\ \frac{\rho_{ij}^2 + \eta h_{ij}^2}{\mathbf{r}_{ij}^2 + \eta h_{ij}^2} & \mathbf{v}_{ij} \cdot \mathbf{r}_{ij} \geq 0 \\ 0 & \mathbf{v}_{ij} \cdot \mathbf{r}_{ij} \geq 0 \end{cases} \quad (21)$$

A new velocity factor is led in as

$$\Phi_{ij}^{(\text{PECM})} = \delta h_{ij} (p_i - p_j) \mathbf{r}_{ij} / (\mathbf{r}_{ij}^2 + \theta h_{ij}^2) / c_{ij} / \rho_{ij} \quad (22)$$

Here  $\alpha, \beta, c_{ij}, \rho_{ij}, h_{ij}, \mu_{ij}, \zeta_{ij}$  are the same in SPH,  $\delta, \theta$  are constants and  $\hat{\rho}_{ij} = \rho_i \rho_j / (\rho_i + \rho_j)$ .

#### C. Discrete Equations

The discrete equations of PECM for mass, momentum and energy, are written in (23) – (25).

$$\frac{d\rho_i}{dt} = \rho_i \sum_{j=1}^N b_j (\mathbf{v}_{ij} + \Phi_{ij}^{(\text{PECM})}) \cdot \nabla_i W_{ij}^{(\text{RKPM})} \quad (23)$$

$$\frac{dv_i}{dt} = -\sum_{j=1}^N b_j (p_j + \Pi_{ij,1}^{(PECM)}) \nabla_i W_{ij}^{(PECM)} \quad (24)$$

$$\frac{de_i}{dt} = \frac{1}{\rho_i} \sum_{j=1}^N b_j [(p_i + \Pi_{ij,2}^{(PECM)}) (v_{ij} + \Phi_{ij}^{(PECM)}) + H_{ij}^{(PECM)}] \cdot \nabla_i W_{ij}^{(RKPM)} \quad (25)$$

#### D. Better Consistencies with Physics

Aimed at essentially improving the consistencies of mathematics with physics, from which an intensive robustness and a high accuracy can be expected, the numerical scheme of PECM has been reconstructed. Comparing with SPH and its derivative methods, PECM has three kinds of modifications such as:

1) *Kernel functions*: Kernels for equations of mass and energy keep unchanged, whereas for momentum equation, a new kernel is introduced considering the harmonious movements of the material cluster comprised of neighbouring clouds, which may have great differences in density with each other. In fact, there is an equation of strain compatibility for continuous mediums, but it does not appear in the governing equations. For mesh-based methods, it is automatically observed as the moving of meshes is dominated by nodes. For the existing meshfree methods like SPH, the particles with smaller density have greater trend to change their velocities than those with larger density, so the equation of strain compatibility is easily to be destroyed especially when strong gradients of density and pressure exist. With the new kernel, containing density, PECM does not update velocity of each cloud in an isolated manner, but felicitously reflects the moving consistency of the neighboring clouds, this may be the uppermost contribution for PECM to have excellent performances in robustness and accuracy.

2) *Modularizing factors*: Being firstly created by PECM, the velocity factor and the second pressure factor were designated according to the laws of interaction between clouds, in which the pressure and velocity should keep continuity macroscopically and the impact force that contribute to inner energy should be dominated mainly by the matter with lower density. These two factors can effectively eliminate the nonphysics results such as numerical oscillations and wall heating.

3) *Discrete equations*: In equations of mass and energy, variables like mass, density and pressure of clouds are withdrawn out of the acting domain of kernel operator. This can help PECM to prevent numerical dissipations in density or energy etc., and the numerical computations can accurately predict the flow fields even they objectively have very abrupt distributions in space.

### V. CODE VERIFICATION OF PECM

The code verification of PECM is depicted as follows.

#### A. Techniques of Code Verification

Stability and accuracy are the most important concerned of numerical methods. In code verification, we assess the

credibility of PECM with three modes: the first is to observe the computing stability based on the dynamic videos formed by numerical results at different times; the second is to inspect the accuracy by comparison between numerical and exact results, good agreement means high accuracy; the third is to quantify the accuracy order based on the decreasing trends of numerical errors when discrete scales diminish. As the space limit, this paper just shows the agreements between the numerical and exact results via static figures.

#### B. Results of Code Verification

In this paper, five models are typically selected to exhibit the advantages of PECM by comparing its numerical results with those of RKPM and the exact solutions. The parameters for initial states in entity models, physics models and numerical computations are listed in Table I - III, respectively, where  $\Delta X$  is the initial discrete scale of clouds and EOS is the abbreviation for equation of state. The numerical results corresponding these parameters are showed in Figure 1-5, where different colors are just used to help the readers easily distinguishing the left or right district each cloud belongs to.

Model 1 aims to verify if the codes are correctly compiled. As all the left and right districts are of same material forming a properly symmetric impact, this model is fit to diagnose code bugs as it is not apt to deeply reveal shortcomings of numerical methods. Figure 1 shows both RKPM and PECM give results that generally agree with exact results, but PECM is more accurate than RKPM, especially in the space near impact interfaces where the shock may lead to discontinuities in density and pressure. Although discontinuity exists just in velocity, we can still observe the deficiencies of RKPM from the numerical results, in which the density decline induced by the wall heating could not be compensated quickly, and the effect of energy smearing made by artificial heat flux can lead to overestimated energy behind the shock wave. In the numerical results, we also see that the velocity factor in (22) can help PECM to eliminate wall heating where strong impact exists.

Model 2 corresponds to a state of dynamic equilibrium and based on physics theory, this equilibrium will keep unchanged forever. This model is built aiming to prove the PECM kernel is more reasonable than RKPM kernel for momentum equation and, the kernel approximation should not act on mass, density and pressure in equations of mass and energy like RKPM does. As the initial state has unified distributions in pressure and velocity, there is no driving force to make material accelerated, so the discontinuities exist in density, energy and EOS can be used exclusively to assess if the numerical schemes have the ability to restrain the errors from generating and developing. Figure 2 shows that PECM gives results free of any errors whereas RKPM leads to illusive error waves.

Model 3 imitates a high pressure explosive impacting a low pressure heavy metal, which is a typical situation in anti-armor weapons or detonation systems especially when nuclear fissions exist. In this model the initial ratio between pressure and density, namely  $p_0/\rho_0$ , is  $(3.5 \times 10^{10})/(2.5 \times 10^3) =$

$1.4 \times 10^7$  for left district and  $0/(2.0 \times 10^4) = 0$  for right district, the ratio of  $p_0/\rho_0$  between the two sides is  $1.4 \times 10^7/0 = \infty$ . The extremely large discrepancy of  $p_0/\rho_0$  across the material interfaces may induce severe instability for RKPM. We have tried many ways to control the evolution of smoothing length in RKPM but interface separation occurs inevitably. In Figure 3 we can see the interface separation and very large errors of RKPM, whereas PECM gives the results well agreed with exact solutions. The new kernel for momentum equation contributes the most to improve the stability and accuracy of PECM; in addition, the modularizing factor for velocity in (22) benefits the PECM to restrain the numerical oscillations.

Model 4 imitates a high pressure heavy metal impacting a low pressure thin gas, which is another typical situation in detonation systems especially when nuclear fusions exist. In this model the ratio of  $\rho_0$  between the two sides reaches  $1.0 \times 10^5$ . The extremely strong discontinuity with density and pressure calls out another baptism for meshfree methods. For this model, RKPM is not able to keep the computation going on as the acute numerical oscillation makes the density and energy less than zero. The numerical results of RKPM in Figure 4 were obtained by the help of artificial controls in time steps and smoothing lengths. Despite the artificial measures used by RKPM, the computation was still unstable and many particles flew off the computational domain, and that the particles left in the domain presented a disordered distribution which implied very large deviations with exact solutions. Simulations of this model are very difficult to keep stable and accurate even for the numerical methods with meshes, but PECM still exported results according well with the exact solutions. Numerical tests of this model indicate that the kernel function in (16) ensures PECM to be stable and accurate, and the second pressure factor in (20) is absolutely necessary to eliminate the nonphysics wall heating especially when very large density ratio exists.

In Model 5, the discontinuity of the initial velocity makes the materials of the two districts rapidly moving apart from each other. As the velocities are high enough, the materials are expanded entirely and vacuum occurs between the two districts. Owing to instability, RKPM gives the results as in Figure 5 by constraining the evolution of smoothing length within 3 times the initial value, from which we still see the

large deviations with exact solutions, whereas PECM can exactly predict the interface separation that exists in reality. As the modularizing factors for pressure and heat flux do not work in this situation, the reform of discrete equations, in addition with the newly introduced kernel and velocity factor may be the most important contributors for PECM to keep excellent stability and accuracy.

Through a large number of numerical tests with various models, we have got adequate evidences indicating that PECM is of super stability and accuracy even with series kinds of strong discontinuities and, the accuracy order is the second for continuous models or lower than the first for most discontinuous problems.

## VI. CONCLUSIONS

The deficiencies of SPH and its derivative methods may be easily exposed when they are applied in the models with strong detonations and shock waves. As there are no concrete geometries of the discrete bodies in meshfree methods, it is very difficult to construct mathematic schemes which can sufficiently reach the physical mechanisms hidden between the discrete bodies disorderly scattered in space. So it is very important to unearth these potential mechanisms and reflect them in the meshfree numerical schemes.

The practice to add density into kernel function for momentum equation may contribute the most for PECM to make clouds moving harmoniously, and this is very important in developing meshfree schemes, for which no vertexes of micro-bodies could be described to prevent the undefined boundaries from splitting and overlapping.

The modularizing factors and the forms of discrete equations in PECM also have great contributions for computing stability and accuracy, which are designed according to the physical mechanisms apparently or recessively existed in the arbitrarily spread clouds which have no perfect geometries.

The properties such as consistency, stability and accuracy are usually difficult to be theoretically proved but, by posteriori assessments in this paper, PECM has achieved enough evidences for its excellent properties.

## ACKNOWLEDGMENT

The author thanks CAEP Foundation (CX2019026) to partially support the works in this paper.

TABLE I. PARAMETERS FOR INITIAL STATES IN ENTITY MODELS

District	Model	Density/kg.m <sup>-3</sup>	Energy/J.kg <sup>-1</sup>	Pressure/Pa	Velocity/m.s <sup>-1</sup>
Left	1	$2.500 \times 10^3$	$6.496 \times 10^6$	$3.500 \times 10^{10}$	$1.500 \times 10^3$
	2	$2.000 \times 10^3$	$5.000 \times 10^6$	$2.000 \times 10^{10}$	$2.000 \times 10^3$
	3	$2.500 \times 10^3$	$7.000 \times 10^6$	$3.500 \times 10^{10}$	0.000
	4	$2.000 \times 10^{-1}$	$1.000 \times 10^7$	$1.000 \times 10^6$	0.000
	5	$2.500 \times 10^3$	$6.496 \times 10^6$	$3.500 \times 10^{10}$	$-7.000 \times 10^3$
Right	1	$2.500 \times 10^3$	$6.496 \times 10^6$	$3.500 \times 10^{10}$	$-1.500 \times 10^3$
	2	$2.000 \times 10^4$	$2.500 \times 10^5$	$2.000 \times 10^{10}$	$2.000 \times 10^3$
	3	$2.000 \times 10^4$	0.000	0.000	0.000
	4	$2.000 \times 10^4$	$2.500 \times 10^5$	$2.000 \times 10^{10}$	$-1.500 \times 10^3$
	5	$2.000 \times 10^3$	$2.400 \times 10^6$	$2.500 \times 10^{10}$	$7.000 \times 10^3$

TABLE II. PARAMETERS OF PHYSICS MODELS

District	Model	EOS Form	$c_0^2/m^2.s^2$	$\rho_0/kg.m^{-3}$	$\gamma$
Left	1	$p = c_0^2(\rho - \rho_0) + (\gamma - 1)\rho e$	$3.600 \times 10^6$	$1.800 \times 10^3$	3.000
	2	$p = c_0^2(\rho - \rho_0) + (\gamma - 1)\rho e$	$2.250 \times 10^6$	$2.000 \times 10^3$	3.000
	3	$p = (\gamma - 1)\rho e$	0.000	0.000	3.000
	4	$p = (\gamma - 1)\rho e$	0.000	0.000	1.500
	5	$p = c_0^2(\rho - \rho_0) + (\gamma - 1)\rho e$	$3.600 \times 10^6$	$1.800 \times 10^3$	3.000
Right	1	$p = c_0^2(\rho - \rho_0) + (\gamma - 1)\rho e$	$3.600 \times 10^6$	$1.800 \times 10^3$	3.000
	2	$p = c_0^2(\rho - \rho_0) + (\gamma - 1)\rho e$	$2.500 \times 10^7$	$2.000 \times 10^4$	5.000
	3	$p = c_0^2(\rho - \rho_0) + (\gamma - 1)\rho e$	$1.500 \times 10^7$	$2.000 \times 10^4$	5.000
	4	$p = c_0^2(\rho - \rho_0) + (\gamma - 1)\rho e$	$2.500 \times 10^7$	$2.000 \times 10^4$	5.000
	5	$p = c_0^2(\rho - \rho_0) + (\gamma - 1)\rho e$	$2.500 \times 10^6$	$1.600 \times 10^3$	6.000

TABLE III. PARAMETERS OF NUMERICAL COMPUTATIONS

$\Delta X/mm$	$h_0/mm$	$n_c$	$\tau$	$\alpha$	$\beta$	$\epsilon$	$g_1$	$g_2$	$\eta$	$\delta$	$\theta$
1.00	1.5	0.00	0.10	1.00	2.00	0.01	1.00	1.00	0.01	0.10	0.01

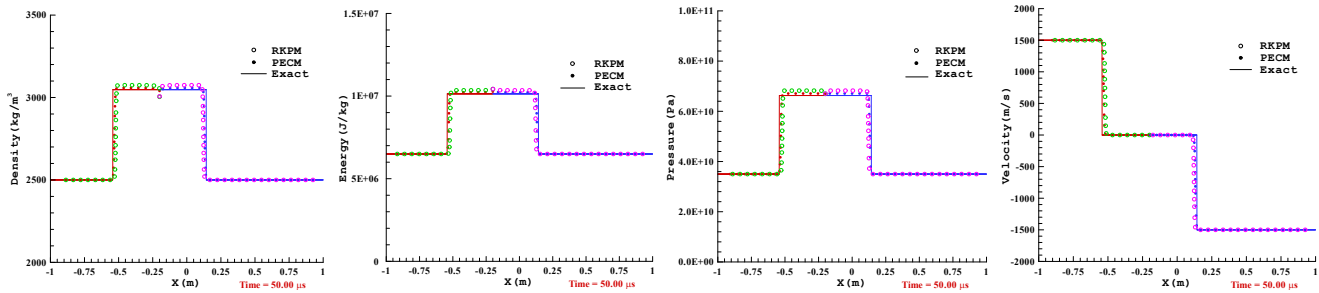


Figure 1. Numerical results about model 1.

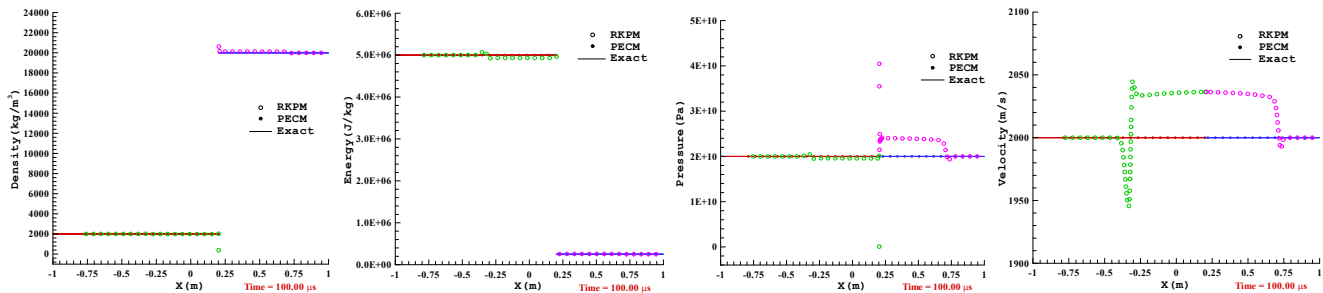


Figure 2. Numerical results about model 2.

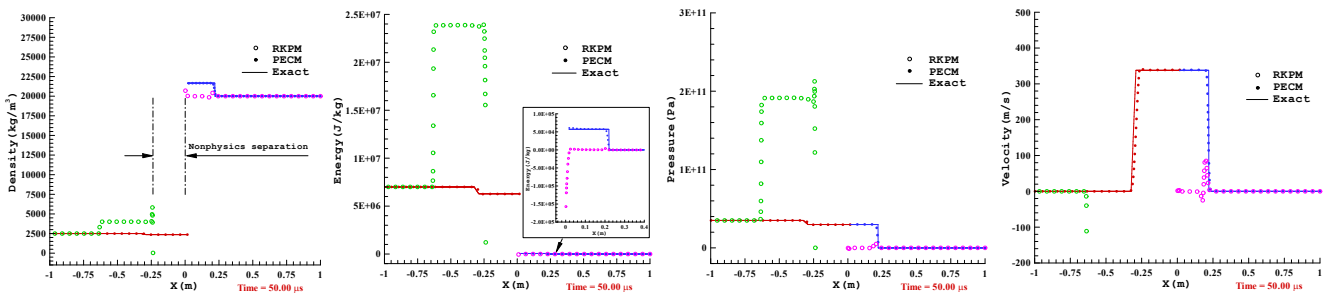


Figure 3. Numerical results about model 3.

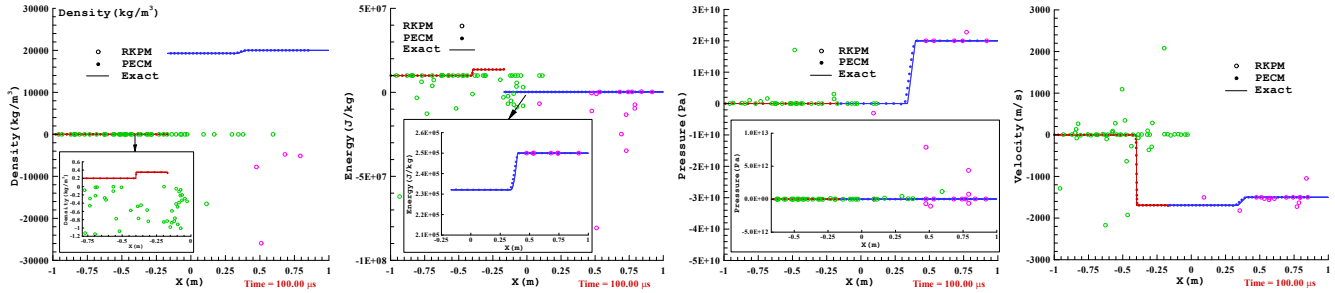


Figure 4. Numerical results about model 4.

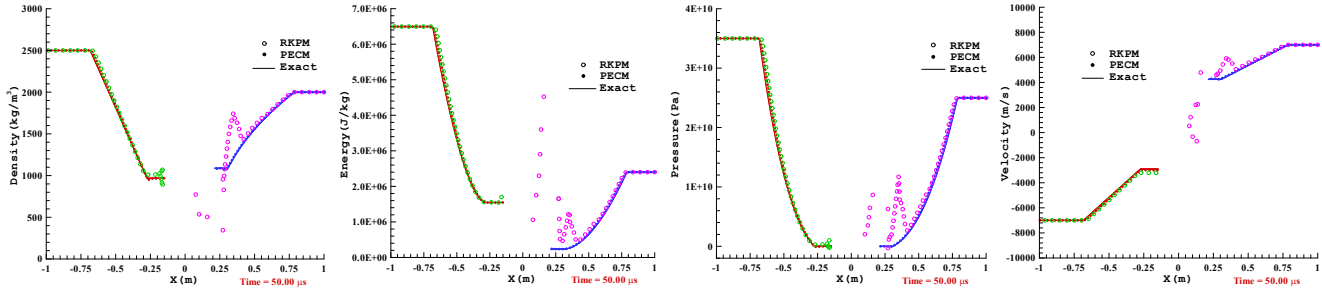


Figure 5. Numerical results about model 5.

REFERENCES

- [1] W. L. Oberkampf and C. J. Roy, "Verification and validation in science computing," Cambridge, UK: Cambridge University Press, 2010.
- [2] Z. B. Ma, Y. T. Sun, and J. W. Yin, "QMU Decision based on modeling & simulation," Chinese Journal of Computational Physics, vol. 33, no. 6, pp. 661-670, 2016.
- [3] J. VonNeumann and R. D. Richtmyer, "A method for the numerical calculation of hydrodynamic shocks," Journal of Applied Physics, vol. 21, no. 3, pp. 232-237, 1950.
- [4] S. K. Godunov, "A finite difference method for the computation of discontinuous solutions of the equations of fluid dynamics," Mathematics of the USSR-Sbornik, vol. 47, pp. 357-393, 1959.
- [5] R. A. Gingold and J. J. Monaghan, "Smoothed particle hydrodynamics: Theory and application to non-spherical stars," Monthly Notices of the Royal Astronomical Society, vol. 181, no. 2, pp. 375-389, 1977.
- [6] L. B. Lucy, "A numerical approach to the testing of the fission hypothesis," Astronomical Journal, vol. 82, no. 12, pp. 1013-1024, 1977.
- [7] W. K. Liu, S. Jun, and S. F. Li, "Reproducing kernel particle methods for structural dynamics," International Journal for Numerical Methods in Engineering, vol. 38, no. 10, pp. 1655-1679, 1995.
- [8] J. K. Chen, J. E. Beraun, and C. K. Jih, "An improvement for tensile instability in smoothed particle hydrodynamics," Computational Mechanics, vol. 23, no. 4, pp. 279-287, 1999.
- [9] G. M. Zhang and R. C. Batra, "Modified smoothed particle hydrodynamics method and its application to transient problems," Computational Mechanics, vol. 34, no. 2, pp. 137-146, 2004.
- [10] Z. B. Ma, "Physics evoked cloud method: a versatile systematic method for numerical simulations," Chinese Journal of Computational Physics, vol. 34, no. 3, pp. 261-272, 2017.
- [11] Z. B. Ma and Y. Z. Zhao, "Code verification of mesh free method with computation of derivatives," Journal of Aerospace Power, vol. 32, no. 8, pp. 1886-1899, 2017.
- [12] Z. B. Ma and Y. Z. Zhao, "Physics evoked cloud method," International Journal of Computational Method, vol. 15, no. 3, pp. 1846006.1-1846006.20, 2018.
- [13] Z. B. Ma and Y. Z. Zhao, "Verification and validation of common derivative terms approximation in meshfree numerical scheme," Journal of Applied and Computational Mechanics, vol. 4, no. 3, pp. 231-244, 2018.
- [14] Z. B. Ma, L. Shi, M. Yu, and H. Zheng, "Code verification of physics evoked cloud method for compressible fluid dynamics," Journal of Aerospace Power, vol. 34, no. 6, pp. 1253-1272, 2019.

# Uncertainty Quantification of Density Reconstruction in High-Energy X-ray Radiography

Haibo Xu

Institute of Applied Physics and  
Computational Mathematics  
Beijing, P.R. China  
Email: xu\_haibo@iapcm.ac.cn

Xingge Li

Institute of Applied Physics and  
Computational Mathematics  
Beijing, P.R. China  
Email: lixingge@lsec.cc.ac.cn

**Abstract**—High-energy X-ray radiography is a measuring technique for quantitative diagnosis of the object and its internal structure. Tomographic reconstruction determines the geometric and physical properties of the object according to the energy distribution on the imaging plane. Considering the noise and blur in the process of radiographing, we construct a general reconstruction model for the axisymmetric single image photographic system. This inverse problem is then cast within a statistical framework in order to compute volumetric object densities from X-ray radiographs and to quantify uncertainties in the reconstruction. A hierarchical Bayesian model is developed with a likelihood based on a Gaussian noise model and with priors placed on the unknown nonnegative density profile, the precision matrix, and two scale parameters. This results in a joint posterior distribution, which can be readily sampled using the Markov chain Monte Carlo (MCMC) method. To study the role of hyperparameters and their sensitivity analysis, a wide variety of tests were conducted which led to a number of definitive conclusions. Results of the density reconstructions and pointwise uncertainty estimates are presented for simulated signals with various physical factors in the imaging process included.

**Keywords**—inverse problem; density reconstruction; uncertainty quantification; Bayesian inference; MCMC method.

## I. INTRODUCTION

High-energy X-ray radiography measures the spatial density distribution of the object, which is of great significance for studying the compression behavior of the object subjected to powerful shocks under the effect of explosives. In this paper, we focus on the problem of uncertainty quantification of density reconstruction for high-energy X-ray radiography. Bayesian formulations for inverse problems have gained considerable attention in the inverse problems community for their utility in uncertainty quantification [1]–[7]. In the application here, we seek an unknown that contains discontinuities but we do not precisely know the discontinuity locations, so we develop a hierarchical Bayesian model for localizing the discontinuities and computing object densities simultaneously. The Bayesian approach combines the prior knowledge of the unknown parameters and the forward model to yield a posterior probability distribution of the model parameters. In this way, the unknown parameters can be characterized by their posterior distributions. The posterior distributions are typically not of analytical form or from a standard parametric family, and characterizing them exactly requires optimization algorithms [8]–[11] or sampling approaches such as MCMC [12].

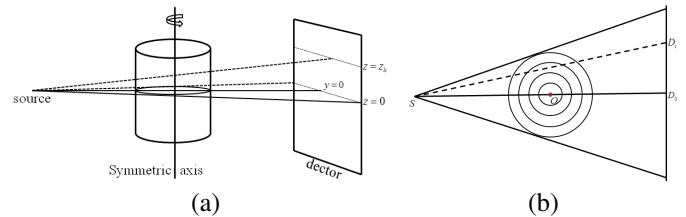


Figure 1. Illustration to single radiographic imaging system for radially symmetric object in 3D view (a) and 2D view (b).

In our experimental setting, a radially symmetric object with radius  $R$  and height  $H$  is situated so that its center-layer lies in the  $xy$ -plane and its axis of symmetry coincides with the  $z$ -axis (see Figure 1(a)). Only a single radiograph is taken with a radiographic axis perpendicular to the symmetric axis of the object. The transmitted radiation is measured by a detector lying on a plane  $x = x_0$ . The X-ray source is placed sufficiently far from the object compared to its size, so that the X-rays can be assumed to be parallel on different layers. In each layer, we consider that the X-rays form a fan-beam shape, see Figure 1(b). Each cross section of the object is projected onto a line of the detector plane. We formulate the density reconstruction model as

$$\mathbf{b} = \mathbf{K}\mathbf{A}\boldsymbol{\rho} + \boldsymbol{\varepsilon}, \quad (1)$$

where  $\mathbf{b} \in \mathbb{R}^m$  is the areal density values,  $\boldsymbol{\rho} \in \mathbb{R}^n$  is the object radial density values,  $\boldsymbol{\varepsilon} \in \mathbb{R}^m$  is unknown noise,  $\mathbf{K}$  presents the blurring that may be produced in the process of radiographing, and  $\mathbf{A} \in \mathbb{R}^{m \times n}$  denotes the forward projection matrix.

The rest of the paper is organized as follows. Section II discusses how to estimate the object density and its corresponding uncertainty quantitatively. Uncertainty quantification of the French Test Object (FTO) reconstruction are presented in Section III, as well as the parameter selection method and sensitivity study. Finally, the conclusion and outlook are given in Section IV.

## II. BAYESIAN FORMULATION OF RECONSTRUCTION PROBLEM

In this section, we introduce a hierarchical Bayesian model to compute object densities and quantify their corresponding

uncertainties at the same time. By selecting conjugate prior distributions, the final posterior formulation can be easily and efficiently sampled using a Gibbs sampler, a specialized MCMC method.

### A. Hierarchical Bayesian model

Since the noise distribution in areal density space is difficult to estimate, we begin with the standard additive Gaussian noise model [13], [14], i.e.,  $\varepsilon \sim \text{Normal}(\mathbf{0}, (\lambda \mathbf{I})^{-1})$  with precision  $\lambda$ . Then the conditional probability density of  $\mathbf{b}$  given the information of  $\boldsymbol{\rho}$  and  $\lambda$ , would be

$$p(\mathbf{b}|\boldsymbol{\rho}, \lambda) \propto \lambda^{n/2} \exp\left(-\frac{\lambda}{2} \|\mathbf{K}\mathbf{A}\boldsymbol{\rho} - \mathbf{b}\|^2\right). \quad (2)$$

Assume that the prior model for  $\boldsymbol{\rho}$  is also a Gaussian,

$$\boldsymbol{\rho} \sim \text{Normal}(\mathbf{0}, (\delta \mathbf{L})^{-1}),$$

where  $\mathbf{L} \in \mathbb{R}^{n \times n}$  is referred to as the precision matrix, and  $\delta > 0$  and  $\mathbf{L}$  are poorly known. Hence, we write a conditional prior for  $\boldsymbol{\rho}$ , assuming that  $\delta$  and  $\mathbf{L}$  were known, as

$$p(\boldsymbol{\rho}|\delta, \mathbf{L}) \propto \delta^{n/2} |\mathbf{L}|^{1/2} \exp\left(-\frac{\delta}{2} \boldsymbol{\rho}^T \mathbf{L} \boldsymbol{\rho}\right),$$

that is, the prior density is conditioned on the knowledge of  $\delta$  and  $\mathbf{L}$ . In consideration of the nonnegativity of density value  $\boldsymbol{\rho}$ , we impose nonnegativity constraint on the computed samples. Suppose  $\mathcal{I} = \mathcal{I}(\boldsymbol{\rho}) \stackrel{\text{def}}{=} \{i|\rho_i = 0\}$  is the zero set and  $p(\mathcal{I})$  a probability model for  $\mathcal{I}$ . Then the prior will depend upon the zero set. If we define  $\mathbf{C}$  to be the diagonal matrix with diagonal entries  $c_{ii} = 1$  for  $i \notin \mathcal{I}$ , and  $c_{ii} = 0$  otherwise, the prior in the unconstrained case is modified as follows:

$$p(\boldsymbol{\rho}|\delta, \mathbf{L}, \mathcal{I}) \propto \delta^{n_p/2} |\mathbf{L}|^{1/2} \exp\left(-\frac{\delta}{2} \boldsymbol{\rho}^T \mathbf{C} \mathbf{L} \mathbf{C} \boldsymbol{\rho}\right), \quad (3)$$

where  $n_p = n - |\mathcal{I}|$ , i.e., the number of positive elements in  $\boldsymbol{\rho}$ .

Assume further that we have a hyperprior density  $p(\mathbf{L})$  for the precision matrix  $\mathbf{L}$ . We suppose here that this density is a Wishart distribution, which is often used for inverse covariance matrices [15]. Thus  $\mathbf{L} \sim \text{Wishart}(\Sigma, \nu)$ , with probability density function

$$p(\mathbf{L}) = \frac{1}{2^{\nu n/2} |\Sigma|^{\nu/2} \Gamma_n(\nu/2)} |\mathbf{L}|^{\frac{\nu-n-1}{2}} \exp\left(-\frac{1}{2} \text{tr}(\Sigma^{-1} \mathbf{L})\right), \quad (4)$$

where  $\Sigma$  is a positive definite scale matrix, and  $\nu$  is the degrees of freedom parameter.

Last, a Gamma hyperprior distribution is chosen for both scale parameters  $\lambda$  and  $\delta$  so that

$$p(\lambda) \propto \lambda^{\alpha_\lambda - 1} \exp(-\beta_\lambda \lambda), \quad (5)$$

$$p(\delta) \propto \delta^{\alpha_\delta - 1} \exp(-\beta_\delta \delta), \quad (6)$$

that is,  $\lambda \sim \text{Gamma}(\alpha_\lambda, \beta_\lambda)$ ,  $\delta \sim \text{Gamma}(\alpha_\delta, \beta_\delta)$ , where  $\alpha_\lambda$  and  $\alpha_\delta$  are Gamma shape parameters and  $\beta_\lambda$  and  $\beta_\delta$  are Gamma rate parameters.

Considering now all  $\boldsymbol{\rho}$ ,  $\lambda$ ,  $\delta$ ,  $\mathbf{L}$  and  $\mathcal{I}$  as unknowns, we write Bayes' formula conditioned on  $\mathbf{b}$  as

$$p(\boldsymbol{\rho}, \lambda, \delta, \mathbf{L}, \mathcal{I}|\mathbf{b}) \propto p(\mathbf{b}|\boldsymbol{\rho}, \lambda, \mathcal{I}) p(\boldsymbol{\rho}|\delta, \mathbf{L}, \mathcal{I}) p(\mathbf{L}) p(\delta) p(\mathcal{I}) p(\lambda),$$

which allows us to estimate  $\boldsymbol{\rho}$ ,  $\lambda$ ,  $\delta$  and  $\mathbf{L}$  simultaneously:

$$\boldsymbol{\rho}|\lambda, \delta, \mathbf{L}, \mathcal{I}, \mathbf{b} \sim \text{Normal}(\mathbf{B}_{\mathcal{I}}^\dagger \lambda \mathbf{A}^T \mathbf{K}^T \mathbf{b}, \mathbf{B}_{\mathcal{I}}^\dagger), \quad (7)$$

$$\lambda|\boldsymbol{\rho}, \delta, \mathbf{L}, \mathcal{I}, \mathbf{b} \sim \text{Gamma}(m/2 + \alpha_\lambda, \frac{1}{2} \|\mathbf{K}\mathbf{A}\boldsymbol{\rho} - \mathbf{b}\|^2 + \beta_\lambda), \quad (8)$$

$$\delta|\boldsymbol{\rho}, \lambda, \mathbf{L}, \mathcal{I}, \mathbf{b} \sim \text{Gamma}(n_p/2 + \alpha_\delta, \frac{1}{2} \boldsymbol{\rho}^T \mathbf{L} \boldsymbol{\rho} + \beta_\delta), \quad (9)$$

$$\mathbf{L}|\boldsymbol{\rho}, \lambda, \delta, \mathcal{I}, \mathbf{b} \sim \text{Wishart}((\Sigma^{-1} + \delta(\boldsymbol{\rho}\boldsymbol{\rho}^T)_{\mathcal{I}})^{-1}, \nu + 1), \quad (10)$$

where  $\mathbf{B} = \lambda \mathbf{A}^T \mathbf{K}^T \mathbf{K} \mathbf{A} + \delta \mathbf{L}$ ,  $\mathbf{D}_{\mathcal{I}} \stackrel{\text{def}}{=} \mathbf{C} \mathbf{D} \mathbf{C}$  and  $\dagger$  denotes pseudo-inverse. Since  $\mathbf{C}\boldsymbol{\rho} = \boldsymbol{\rho}$  (recall that  $\rho_i = 0$  for  $i \in \mathcal{I}$ ), equivalent distributions result if  $\mathbf{C}$  is removed in (8),  $\mathbf{L}_{\mathcal{I}}$  is replaced by  $\mathbf{L}$  in (9), and  $(\boldsymbol{\rho}\boldsymbol{\rho}^T)_{\mathcal{I}}$  is substituted as  $\boldsymbol{\rho}\boldsymbol{\rho}^T$  in (10). We do this in what follows.

It remains to define  $p(\mathcal{I})$  and the conditional density  $p(\mathcal{I}|\boldsymbol{\rho}, \lambda, \delta, \mathbf{L}, \mathbf{b})$ . This can be accomplished by computing [1]

$$\hat{\rho} = \arg \min_{\boldsymbol{\rho} \geq \mathbf{0}} \left\{ \frac{1}{2} \boldsymbol{\rho}^T \mathbf{B} \boldsymbol{\rho} - \boldsymbol{\rho}^T (\lambda \mathbf{A}^T \mathbf{K}^T \mathbf{b} + \mathbf{w}) \right\}, \quad (11)$$

where  $\mathbf{w} \sim \text{Normal}(\mathbf{0}, \mathbf{B})$ . That is, solving (11) yields simultaneous samples of both  $\boldsymbol{\rho}$  and, implicitly,  $\mathcal{I}$  from  $p(\mathcal{I}|\boldsymbol{\rho}, \lambda, \delta, \mathbf{L}, \mathbf{b})$ . And, more remarkable, this optimization problem can be easily solved exploiting the Constrained Conjugate Gradient (CCG) method [16]. We still have not defined  $p(\mathcal{I})$ , but this is not necessary to define our MCMC method.

### B. MCMC sampling of the posterior distribution

The power in (7)–(10) lies in the fact that samples from these four distributions can be easily computed using standard statistical software, though nonlinear optimization techniques will be needed for (7). A Gibbs sampler that results from sequential use of the conditional densities  $p(\mathcal{I}|\boldsymbol{\rho}, \lambda, \delta, \mathbf{L}, \mathbf{b})$  and (7)–(10) can be written without an explicit sampling step for  $\mathcal{I}$ . The sampler begins with  $\boldsymbol{\rho}$ , and is initialized with  $\lambda_0$ ,  $\delta_0$ , and  $\mathbf{L}_0$ . A basic outline is listed in Algorithm 1.

---

#### Algorithm 1 (MCMC sampler)

---

1. Select  $\lambda_0$ ,  $\delta_0$  and  $\mathbf{L}_0$ . Select a maximum number of samples,  $N$ , and set  $k = 0$ .
2. Compute

$$\boldsymbol{\rho}^k = \arg \min_{\boldsymbol{\rho} \geq \mathbf{0}} \left\{ \frac{1}{2} \boldsymbol{\rho}^T \mathbf{B}_k \boldsymbol{\rho} - \boldsymbol{\rho}^T (\lambda_k \mathbf{A}^T \mathbf{K}^T \mathbf{b} + \mathbf{w}) \right\},$$

where  $\mathbf{B}_k = \lambda_k \mathbf{A}^T \mathbf{K}^T \mathbf{K} \mathbf{A} + \delta_k \mathbf{L}_k$  and  $\mathbf{w} \sim \text{Normal}(\mathbf{0}, \mathbf{B}_k)$ , using the CCG method.

3. Compute  $\lambda_{k+1} \sim \text{Gamma}(m/2 + \alpha_\lambda, \frac{1}{2} \|\mathbf{K}\mathbf{A}\boldsymbol{\rho}^k - \mathbf{b}\|^2 + \beta_\lambda)$ .
4. Compute  $\delta_{k+1} \sim \text{Gamma}(n_p^k/2 + \alpha_\delta, \frac{1}{2} (\boldsymbol{\rho}^k)^T \mathbf{L}_k \boldsymbol{\rho}^k + \beta_\delta)$ , where  $n_p^k$  is the number of positive entries in  $\boldsymbol{\rho}^k$ .
5. Compute

$$\mathbf{L}_{k+1} \sim \text{Wishart}((\Sigma^{-1} + \delta_{k+1} \boldsymbol{\rho}^k (\boldsymbol{\rho}^k)^T)^{-1}, \nu + 1).$$

6. Set  $k = k + 1$ . If  $k < N$ , return to step 2.
- 

Samples obtained via the above MCMC algorithm are used to compute the sample mean and 95% credibility intervals. The sample mean well characterizes the unknown true density, and the credibility intervals provide uncertainty quantification in the posterior estimate.

### III. NUMERICAL EXPERIMENTS

In this section, we test on a simulated radiograph of the FTO, which is generated by the Monte Carlo N-Particle (MCNP) transport code [17], to demonstrate the ability of MCMC method to reconstruct an axially symmetric object. In this numerical simulation, the source is assumed as a monoenergetic photon beam of 4 MeV, and the source blur is treated as Gaussian, whose full width at half maximum is 0.3 cm. The FTO consists of a set of concentric spheres with a void region at the center. The void has a radius of 1.0 cm. The second layer is tungsten with radius of 4.5 cm and density of 18.9 g/cm<sup>3</sup>. The third layer is copper with radius of 6.5 cm and density of 8.9 g/cm<sup>3</sup>. The FTO is placed 200 cm from the source, and the detector is 250 cm behind the object. Figure 2(a) shows the synthetic radiograph of the total exposure, and Figure 2(b) shows the profiles at the equator of the direct and scattered exposure respectively.

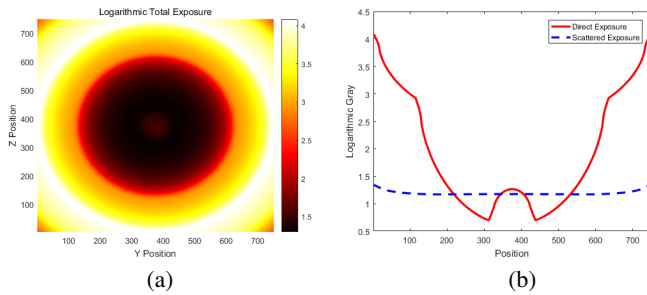


Figure 2. MCNP simulation results of the FTO. (a) Radiograph capturing both direct and scattered radiation; (b) the central cross sections of the direct and scattered exposure.

Obviously, the introduction of the hyperprior distributions in (4)–(6) requires the choice of hyperparameters  $\alpha_\lambda$ ,  $\beta_\lambda$ ,  $\alpha_\delta$ ,  $\beta_\delta$ ,  $\nu$ , and  $\Sigma$ . Setting the MCMC sampler with these hyperparameters and initializations  $\lambda_0$ ,  $\delta_0$  and  $\mathbf{L}_0$ , we computed 100,000 samples and made the last 95,000 available, which demonstrated stationarity and had little correlation between samples [15]. From these samples, we plot the sample mean as our reconstruction, which is known as conditional mean (CM) estimate of the unknown density, and 95% credibility intervals given by the 0.025 and 0.975 quantiles of the samples at each location, which were computed using empirical quantiles.

#### A. Parameter selection

We have to study first the role of hyperparameters. For the hyperparameters  $(\alpha_\lambda, \beta_\lambda)$ , it is easy to see that  $\lambda$  characterises the noise level  $\sigma^2$  of areal density. The smaller the value, the higher the noise. Since the mean and variance of the corresponding Gamma distribution are  $\alpha_\lambda/\beta_\lambda$  and  $\alpha_\lambda/\beta_\lambda^2$  respectively, we choose appropriate  $\alpha_\lambda$  and  $\beta_\lambda$  such that  $\alpha_\lambda/\beta_\lambda$  is close to  $\sigma^{-2}$  and  $\alpha_\lambda/\beta_\lambda^2$  is smaller. In our numerical experiments, we just set  $\alpha_\lambda = \sigma^{-2}$  and  $\beta_\lambda = 1$ .

We now study the effect of the hyperparameters  $(\alpha_\delta, \beta_\delta)$ . To this end, we employ the variable-controlling approach by setting  $\lambda$  and  $\mathbf{L}$  as known. We then fix  $\alpha_\delta = 1$ , and the corresponding Gamma distribution degenerates to an exponential distribution. The maximum a posteriori estimate for the pair  $(\rho, \delta)$  are calculated for various values of  $\beta_\delta$ . We then pick a proper  $\hat{\beta}_\delta$  with good performance of  $\hat{\rho}$ . Similar to  $\lambda$ , we select suitable  $\alpha_\delta$  and  $\beta_\delta$  such that  $\alpha_\delta/\beta_\delta$  is equal to  $1/\hat{\beta}_\delta$

and  $\alpha_\delta/\beta_\delta^2$  is smaller. In our numerical experiments, we just set  $\alpha_\delta = \beta_\delta^{-1}$  and  $\beta_\delta = 1$ .

Last but not least, setting the Wishart degrees of freedom parameter  $\nu = n + 1$  ensures that the distribution is well defined [18] [19]. Since the Wishart has mean  $\nu\Sigma$ , the quality of the final reconstruction is supposed to be greatly improved by choosing a  $\Sigma$  that incorporates edge information. We then set  $\Sigma = \frac{1}{\nu}\mathbf{L}_{TV}(\rho_{TV})$  to center the hyperprior for  $\mathbf{L}$  around the initial edge estimate provided by total variation (TV) solution  $\rho_{TV}$ , where  $\mathbf{L}_{TV}(\rho_{TV}) = \mathbf{D}^T\psi(\rho_{TV})\mathbf{D}$ ,  $\psi(\rho_{TV}) := \text{diag}\left(1/\sqrt{(\mathbf{D}\rho_{TV})^2 + \eta}\right)$ ,  $\eta$  is a small positive constant, and  $\mathbf{D}$  is the forward differencing matrix [15].

#### B. Parameter sensitivity

We now reconstruct the density distribution of the FTO with the resulting areal density from the direct radiation shown in Figure 2(b), and provide a parameter sensitivity analysis for  $\Sigma$  and  $\beta_\delta$ . For the MCMC sampler, the degrees of freedom parameter  $\nu$  is set to be  $n + 1$ , the Wishart scale matrix  $\Sigma$  is computed to be  $\frac{1}{\nu}\mathbf{L}_{TV}(\rho_{TV})$ , and  $\mathbf{L}_{TV}(\rho_{TV})$  is also used for  $\mathbf{L}_0$ . The initial  $\lambda$  and  $\delta$  parameters are drawn from a Uniform(0, 1) distribution. All the remaining parameters for the Gibbs sampler are selected as noted above and are given in Table I.

The sensitivity of the TV solution, which is used to inform the hyperparameter  $\Sigma$ , is tested by providing the sampler with a TV solution that contained no edge information and a TV solution that indicated incorrect edge locations and densities. For ease of comparison, we also calculate the CM estimate, initializing the sampler with a proper TV solution. The mean square error is computed using the mean reconstruction compared to the true density profile of the FTO. As shown in Table I, the mean square error of the original reconstruction is 0.0637392 and each of these two reconstructions differs from that by no more than 0.000002. Both of these reconstructions demonstrate the Bayesian method's ability to overcome a poorly informed  $\Sigma$  parameter, relying on the data to determine edges and density scales.

To understand the sensitivity of the solution to the parameter  $\beta_\delta$ , we carry out reconstruction experiments on the areal density, which is corrupted with Gaussian noise at level 1.5% of maximum of the noiseless projection data. Samples of the MCMC chain are drawn from the conditional distributions, holding all but  $\beta_\delta$  constant and changing  $\beta_\delta$  from  $10^0$  to  $10^1$ . Combined with the mean square error in Table I, we can observe that the MCMC sampler with different  $\beta_\delta$  makes very little difference.

TABLE I. PARAMETERS STATISTICS AND COMPARISON OF MEAN SQUARE ERRORS.

$\alpha_\lambda$	$\beta_\lambda$	$\alpha_\delta$	$\beta_\delta$	$\Sigma$	$\ \rho_{\text{MCMC}} - \rho_{\text{true}}\ /\sqrt{n}$
$10^6$	$10^0$	$10^2$	$10^0$	correct	0.0637392
$10^6$	$10^0$	$10^2$	$10^0$	non	0.0637399
$10^6$	$10^0$	$10^2$	$10^0$	wrong	0.0637404
$7.3 \times 10^5$	$10^0$	$10^2$	$10^0$	correct	0.0636181
$7.3 \times 10^5$	$10^0$	$10^2$	$10^1$	correct	0.0632581

We can summarize from the data in Table I that  $(\alpha_\delta, \beta_\delta)$  can be applicable to the projection data of the same object in different situations, while the selection of  $(\alpha_\lambda, \beta_\lambda)$  is related

to the noise level of the projected data, and different values are obtained for different data.

### C. Uncertainty caused by physical factors

Although empirical knowledge constraints have been added into density reconstruction, it does not eliminate the uncertainty of reconstruction results (11), but only reduces the uncertainty of reconstruction modeling (1), so it is necessary to analyze the factors causing uncertainty in density reconstruction. Generally, there are uncertainties caused by the conversion from optical density to areal density, the noise in areal density, the measurement error of areal density as well as the reconstruction method itself. In our simulation, errors in the reconstruction from the direct radiation data are mainly caused by the noise and measurement error in areal density and our approach to the density reconstruction problem (1).

Images captured by X-ray imaging systems are direct measures of the optical density. The measured optical density,  $G$ , can be converted to areal density,  $b$ , using a measured transmission curve, which is given by

$$G = G_0 + k(X_D + X_S) = G_0 + k \left( \frac{X_0}{d^2} e^{-b} + X_S \right), \quad (12)$$

where  $G$  and  $G_0$  is the optical density and background density at that point;  $k$  is the slope of the transmission curve;  $X_0$  is the radiation exposure;  $d$  is the distance between source and the imaging plane;  $X_S$  is the scattered radiation;  $X_D$  is the direct radiation. The uncertainty of areal density measurement caused by the indeterminacy of scattering irradiation, incident exposure and transmission curve measurements can be summarized as

$$\Delta b = \sqrt{\text{SDR}^2 \left( \frac{\Delta X_S}{X_S} \right)^2 + \left( \frac{\Delta X_0}{X_0} \right)^2 + (1 + \text{SDR})^2 \left( \frac{\Delta k}{k} \right)^2}, \quad (13)$$

where  $\text{SDR} = \frac{X_S}{X_D}$  denotes the ratio of scattering to direct radiation. According to the accuracy of experimental measurement, the error range of physical quantities in (13) can be approximated by

$$\frac{\Delta X_S}{X_S} \leq 10\%, \quad \frac{\Delta X_0}{X_0} \leq 5\%, \quad \frac{\Delta k}{k} \leq 10\%,$$

then we can obtain the measurement error of areal density:

$$\Delta b = 0.1 \sqrt{\text{SDR}^2 + 0.25 + (1 + \text{SDR})^2}. \quad (14)$$

To analyse the uncertainty introduced by noise in the imaging process, we carry out reconstruction experiment on the noisy areal density, which is corrupted with Gaussian noise at level 1.5% of maximum of the noiseless projection data. Compared with the posterior estimation from noiseless data, as shown in Figure 3 (a), credibility interval at every location in (b) becomes obvious when noise added, and all of them are within 10% of the density value there. When comparing the CM estimate with TV estimate, in the terminology of the classical regularization theory one is tempted to say that the former is underregularized compared to the latter. However, from the statistical point of view, the CM estimate is consistent with the prior.

In consideration of the uncertainty in areal density measurement, we impose the correct value  $\Delta b$  on the areal density. Then we run MCMC for the corrected areal densities  $b - \Delta b$

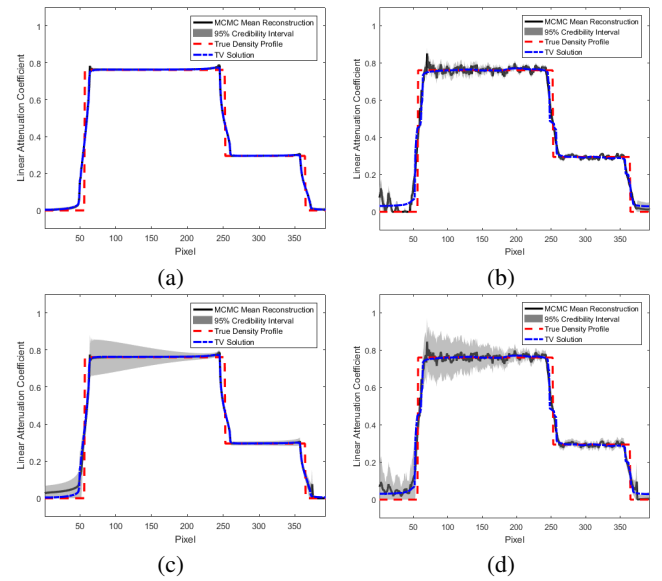


Figure 3. Density reconstructions. (a) Reconstruction results from the noiseless areal density; (b) reconstruction results from the noisy areal density; (c) reconstruction results from the noiseless areal density with correction; (d) reconstruction results from the noisy areal density with correction.

and  $b + \Delta b$  separately. To imitate the density uncertainty caused by measurement uncertainty, these two estimates are merged into single one, as shown in Figure 3 (c), whose density values are average of two estimates, and the pointwise credibility intervals are unions of two original intervals. The mean square error between the density distributions in (c) and (a) is 0.0133972, which verifies the validity of our estimation method. The credible band is tight across the image except for the jump locations.

Considering the uncertainties caused by noise and areal density measurement together, we get the noisy areal density to minus and plus the correction (14) separately, and obtain the corresponding noisy projection data with correction. Based on the previously explained MCMC run, the CM estimates together with credible intervals are shown in Figure 3 (d). It is easy to see that the density distribution in (d) is very close to those in (b), and the mean square error between them is 0.0130941. However, the 95% credibility intervals become wider with the introduction of correction, particularly around the boundary of inner layers, and this is consistent with the case in (c). In each example illustrated above, the uncertainty is seen to be lower near regions of constant density in the reconstruction and higher near edge locations.

## IV. CONCLUSION

In this paper, a generalized density reconstruction model is presented based on the assumption that noise and blur will occur during the imaging process. Then, a hierarchical Bayesian model is proposed for computing object densities and estimating their uncertainties simultaneously. Density samples drawn from the conditional posterior distribution are insensitive to the choice in hyperparameter values selected based on the model. Numerical experiments indicate that our MCMC method achieves quite effective reconstruction results and is comparable to TV regularization. Moreover, the uncertainty

of density reconstruction is mainly introduced by noise and measurement error of physical quantities in the process of radiography.

In this paper, the X-rays are assumed to be parallel on different layers, and they form a fan-beam shape in each layer. In the future, we plan to estimate the uncertainty of cone beam reconstruction using the MCMC method. Furthermore, we will consider other explicit noise models according to the characteristics of experimental data, such as poisson noise, impulse noise and a composition of them. We will also construct the prior density in more ways based on the nature of the prior information, for example,  $\ell^1$  prior, Cauchy density, entropy density, lognormal density, discontinuities prior and so on.

#### ACKNOWLEDGMENT

H. Xu was supported by NSFC Funds (grant No. 11675021). X. Li was supported by National Postdoctoral Program for Innovative Talents (grant No. BX201700038).

#### REFERENCES

- [1] J. M. Bardsley and C. Fox, "An MCMC method for uncertainty quantification in nonnegativity constrained inverse problems," *Inverse Problems in Science & Engineering*, vol. 20, no. 4, pp. 477–498, 2012.
- [2] J. P. Kaipio and E. Somersalo, "Statistical and computational inverse problems," *Technometrics*, vol. 48, no. 1, pp. 146–146, 2005.
- [3] A. M. Stuart, "Inverse problems: A Bayesian perspective," *Acta Numerica*, vol. 19, no. 19, pp. 451–559, 2010.
- [4] L. Tenorio, *Statistical Regularization of Inverse Problems*. Society for Industrial and Applied Mathematics, 2001.
- [5] J. Li and Y. M. Marzouk, "Adaptive construction of surrogates for the bayesian solution of inverse problems," *SIAM Journal on Scientific Computing*, vol. 36, no. 3, pp. A1163–A1186, 2014.
- [6] L. Yan and T. Zhou, "Adaptive multi-fidelity polynomial chaos approach to bayesian inference in inverse problems," *Journal of Computational Physics*, vol. 381, pp. 110–128, 2019.
- [7] L. M. M. V. D. Bos, B. Sanderse, W. A. A. M. Bierbooms, and G. J. W. V. Bussel, "Bayesian model calibration with interpolating polynomials based on adaptively weighted leja nodes," *Communications in Computational Physics*, 2019.
- [8] A. Soares, R. Rabelo, and A. Delbem, "Optimization based on phylogram analysis," *Expert Systems with Applications*, vol. 78, pp. 32–50, 2017.
- [9] M. Shams, E. Rashedi, S. M. Dashti, A. Hakimi, M. Shams, E. Rashedi, S. M. Dashti, and A. Hakimi, "Ideal gas optimization algorithm," *International Journal of Artificial Intelligence*, vol. 15, no. 2, pp. 116–130, 2017.
- [10] R.-E. Precup, *Nature-Inspired Optimization Algorithms for Fuzzy Controlled Servo Systems*. Oxford: Butterworth-Heinemann, 2019.
- [11] B. H. Abed-alguni, "Island-based cuckoo search with highly disruptive polynomial mutation," *International Journal of Artificial Intelligence*, vol. 17, no. 1, pp. 1–29, 2019.
- [12] S. Brooks, A. Gelman, G. L. Jones, and X.-L. Meng, *Handbook of Markov Chain Monte Carlo*. Boca Raton: Chapman & Hall/CRC, 2011.
- [13] D. Calvetti and E. Somersalo, *Introduction to Bayesian scientific computing*. New York: Springer, 2007.
- [14] O. Scherzer, M. Grasmair, H. Grossauer, M. Haltmeier, and F. Lenzen, *Variational Methods in Imaging*. New York: Springer, 2009.
- [15] M. Howard, M. Fowler, A. Luttman, S. E. Mitchell, and M. C. Hock, "Bayesian Abel inversion in quantitative X-ray radiography," *SIAM Journal on Scientific Computing*, vol. 38, no. 3, pp. B396–B413, 2016.
- [16] E. A. H. Vollebregt, "The bound-constrained conjugate gradient method for non-negative matrices," *Journal of Optimization Theory and Applications*, vol. 162, no. 3, pp. 931–953, 2014.
- [17] X. M. C. Team, "MCNP – A general Monte Carlo N-particle transport code, version 5," Los Alamos Nuclear Laboratory, Tech. Rep. LA-UR-03-1987, 2003.
- [18] C. Bishop, *Pattern Recognition and Machine Learning*. New York: Springer, 2006.
- [19] A. Gelman *et al.*, *Bayesian Data Analysis*. Boca Raton: CRC Press, 2013.

# Multi-Factor Authentication for Public Displays using the Semantic Ambient Media Framework

David Bouck-Standen, Josefine Kipke  
Kingsbridge Research Center  
Hamburg, Germany  
email: {dbs, jfk.student}@kingsbridge.eu

**Abstract**—In our interconnected society, public displays deliver private and personalized content. This presents the need to authenticate users in order to protect personal and private information or sensitive contexts of use. In general, authentication mechanisms on public displays are subject to a number of risks, especially, if displays offer multi-touch interfaces or grow even larger. In this contribution, we present a multi-factor authentication system for public displays using the Semantic Ambient Media Framework. In our approach, at first, users use their personal mobile devices, such as smartphones or tablets, to authenticate themselves securely. On the smartphone, a graphical code is displayed, which the user enters on a grid shown on the public display. In a last step, the user confirms the authentication on his smartphone. The code displayed on the smartphone is a one-time and location-based code and no actual credentials have to be typed in on the public display. Thus, this method protects against threats, such as shoulder surfing, thermal attacks, or smudge attacks.

**Keywords**-Multi-factor Authentication; Pervasive Displays; Secure Public Authentication;

## I. INTRODUCTION

Large multi-touch displays are already deployed in public spaces, such as public squares, airports, train stations, or in streets. Public displays consist of large multi-touch displays connected to a content providing system via the Internet. Today however, there is an increasing demand for public displays to offer access to personalized or context-specific content or functionalities [1]. Accessing protected data and contexts on public displays presents the need of a secure method for user authentication.

Authentication in general requires a user to enter credentials or other means for personal identification, only known to or in possession of the user himself. This could be, e.g., classically a username-password combination, or a thumbprint, iris or other biometrical information unique to the user [2].

The increasing use and functionality of public displays require providing a solution that protects against threats. These can be for example *shoulder surfing attacks* (a), where the user is observed while authenticating [3], *thermal attacks* (b), where heat traces resulting from the user's interactions are made visible revealing the sensitive authentication data [4][5], or *smudge attacks* (c) that exploit the residues from finger prints on touch-screens [6]. Research on these

techniques indicate that shoulder surfing occurs in daily contexts [3]. All three attack methods have in common that displaying a digital keyboard or using a software keyboard is vulnerable to them. For this reason and to prevent possible attacks exploiting the users' interactions with the systems, systems for biometrical authentication or gaze-touch have been proposed [7].

Using additional hardware, such as bio-scanners or cameras, for public displays comes with costs and the need to retrofit most public displays currently deployed. A solution with minimal hardware requirements is more likely to be widely accepted. Thus, one of the challenges of this work is to find a solution that does not require hardware upgrades of public displays.

Modern smartphones are personal devices, equipped with different sensors and mostly more than one camera. The smartphone is still on the rise due to its connectivity, as almost 8 out of 10 Internet users in the EU surfed via a mobile or smartphone. The trend toward mobile technology and mobile Internet usage can be observed globally [8].

In this work, we present a technical solution we developed as prototype at the Kingsbridge Research Center (KRC), which addresses these challenges with a minimal technical solution. This makes use of a *multi-factor authentication* (MFA) [2]: The first factor is the *ownership* (i) of a personal mobile device, such as a smartphone. The second factor is *knowledge* (ii) of personal credentials, such as the combination of username and password. Using GPS data, we also use the users and display's *location* (iii) as third factor.

The concept of this work makes use of the interconnectedness of the devices through the Internet, using the Semantic Ambient Media Framework (SAM.F) [9] as an authoritative interface between smartphones and public displays.

In this contribution, we regard related work in Section 2, and present a practical scenario in Section 3. In Section 4, we outline the systems concept and architecture and describe our prototype implementation. In the final section, we summarize our work and illustrate future work.

## II. RELATED WORK

This work takes place in the research field of public displays. Related work indicates a general increase in the deployment of public displays [10]. Today, public displays are widely connected in client-server-applications for content

serving purposes, and they are connected through the Internet [10]. For example, Memarovic et al. focus on interconnecting displays, e.g., with social media [11]. Our work ties onto related work through its modular client-server-based architecture. As this work depends on Web-based and modular technology, it can be integrated into existing projects.

Another research field of interest is the field multi-factor authentication, as recently surveyed by Ometov et. al [2]. Ometov et. al outline state of the art methods for MFA, illustrate technical requirements, and identify commercial, governmental, and forensic applications as three market-related groups of applications for MFA. In context with public displays, this work can potentially be deployed in all three field, but the use in commercial applications is most likely.

One of the main challenges of MFA is the absence of a correlation between the user identity and the identities of smart sensors and systems or devices, as Ometov et. al observe [2]. They propose a user-friendly process to establish a trust relationship to gain access rights, whereas Mannan et. al [12] propose a concept to use a personal device to strengthen password authentication from untrusted computers. We apply these theoretical approaches to our technically limited setting, as outlined above, and present a feasible solution for the MFA for public displays using SAM.F.

The research field of semantic frameworks is also of value to this contribution. These frameworks are used to model data structures and interconnect media with applications, services and devices [9][13][14].

With the system called Tacita, Shaw et. al [10] demonstrate a system to personalize public display experience by utilizing proximity detection for user's mobile devices, e.g., with iBeacon technology. Tacita ubiquitously personalizes public displays' content, whereas GTmoPass proposed by Khamis et. al relies on gaze-touch detection through the smartphone and the identification of the display via a Bluetooth Low Energy (BLE) beacon [7]. These approaches are distinguished from the approach presented in this contribution, as the system we develop directly authenticates users and requires a direct user interaction on the public display. It therefore supports direct use, which features the use of public displays in both unauthenticated, as well as authenticated contexts, especially, if personal information or private functionality is displayed. In addition, the solution proposed in this article does not need any supplementary hardware, such as BLE beacons.

The following scenario illustrates exemplary use-cases for the system proposed in this article.

### III. SCENARIO

Today, a system administrator is servicing the systems of a museum in Hamburg. On the front wall outside the museum, public displays are installed. To carry out his task, he needs to access the systems and log onto the administrator mode. Standing in front of the display, the administrator uses his smartphone to authenticate him. Then, on the smartphone, a code is displayed. On the public screens, the administrator now accesses the login menu and a grid of 9 symbols appears. He enters the code from his smartphone by touching the five symbols in the correct order. A stroller passes by, curiously watching him entering the code, but the administrator is not alarmed, as the public display now shows a hint indicating, that he has to confirm the login on his smartphone. Using his mobile device, the administrator sees a prompt showing the display name and location. He finds this information is correct and confirms the login. Instantly, the public display changes and shows the administrator's dashboard.

The scenario shows an exemplary use case, in which after a successful logon, the administrator can access features that are hidden from unauthenticated users and also from users, who are not assigned to the administrator group. However, this work only focuses on the authentication process. Thus, modeling the use case is subject to the application applying the login to their system.

### IV. SYSTEM CONCEPT AND ARCHITECTURE

For this approach and under consideration of the technical limitations outlined above, the following is the starting point for this work:

- users are in possession of a smartphone or equivalent device connected to the Internet. They have already registered an account with credentials known to SAM.F beforehand, as this is a preliminary requirement of this work.
- public displays are connected to the Internet and run on Web-based technology, e.g., showing Web-based contents in a browser-based system.
- the user sojourns in the vicinity of a public display and intentionally starts a private context.

Figure 1 illustrates the system's architecture and the starting point. In a single location, one or more users and one or more displays can be present. A user interacts with a single display and is in possession of a personal mobile device, as depicted in Figure 1. All public displays and user's devices are connected to SAM.F through the internet. However, a direct connection between a smartphone and any public display does not exist.

Inside SAM.F, the *multi-factor authentication for public displays* (MFA4PD) module is hosted. Public displays and user’s devices connect to the MFA4PD module through the Internet. In addition, public displays connect to external content providers, which are not illustrated in Figure 1, for simplification purposes.

The system’s architecture benefits from the technical limitations outlined above. As there is no direct connection necessary between the personal mobile device of a user and the public display used for authentication, there is no need for the display provider to open up his network for foreign devices. Thus, a multi-device ecology within the network of the display provider is not required, resulting in less administrative effort. From Figure 1, it can also be observed that no additional hardware, such as, e.g., BLE beacons, is required.

The system concept relies on the interconnection of mobile devices and public displays through SAM.F, which is described in Section A. To begin using a personal or private context on a public display, the user completes the authentication process, as illustrated in Section B. We discuss our approach in terms of security in Section C and describe the prototype implementation in Section D.

A. SAM.F

The *Semantic Ambient Media Framework* (SAM.F) we develop at KRC is a framework semantically interconnecting (a) *media*, (b) *devices*, and (c) *services*, which are enriched by digital properties in the form of semantic annotations [9].

In SAM.F, media consists of text, photos, audio, videos, animations, 3D objects, which are extended by digital properties, e.g., by classifying the media’s content using the OWL Web Ontology Language in the internal model of SAM.F.

Digital properties are also Meta data from the original file, such as Meta information on MIME type or encoding. For devices, in SAM.F we model digital properties reflecting, e.g., the devices’ capabilities’, location, capacity or screen size.

All digital properties are used by the services in SAM.F. Using a dedicated application model, an application accesses the services in SAM.F through Web-based interfaces. Each service serves a dedicated purpose, interconnecting applications through the shared use of devices and media.

The architecture of SAM.F, although described here only with reference to the MFA4PD module, consists of a layer-based system concept, as illustrated in Figure 2. A client application, such as the display or mobile application of this work described in more detail below, connect to the SAM.F *API Web Services* through the *API Security Layer*. Data is exchanged between applications and services, which reside in the *Service Logic* layer, in the form provided by the specification of the *API Client Data Model*. Internally, SAM.F works with a dedicated *Data Model*, as illustrated in Figure 2. Any data is mapped from the *Datastore*, which includes external (semantic) databases, as well as binary data stores, to the internal *Data Model*, which applies a homogenous model to potentially heterogenic data. For simplification purposes, and in order to reduce the learning

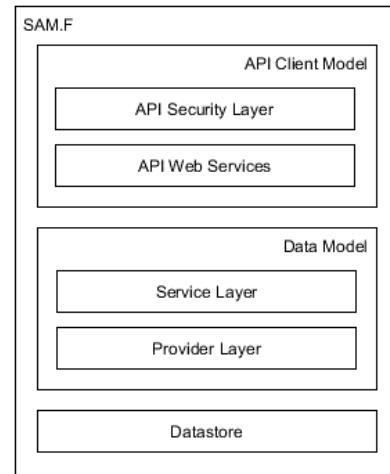


Figure 2. Architecture of SAM.F.

curve when implementing applications accessing SAM.F, the internal *Data Model* is only used in the *Provider Layer*, which contains, e.g., authentication or data providers to be accessed by the upper *Service Layer*, and in the *Service Layer*, as shown in Figure 2. Any data provided by a service to a client is mapped to the specific *API Client Data Model* before being served through the *API Web Services* and the *API Security Layer*.

Applying data mapping in SAM.F produces constant overhead, but services and applications, as well as their developers, benefit from only working with data models that are specific to the requirements of the services’ or applications’ context, reducing overhead when loading large sets of data. Data in this respect describes media, devices and services.

In context of this work, SAM.F serves as authentication provider, which validates user credentials via its standard user service. This work extends the *Service Layer* of SAM.F by adding the MFA4PD module, which implements the authentication process described in the following section.

B. Authentication Process

To start a private session on one of the public displays, the user opens up the *mobile application* of MFA4PD on his personal smartphone. The user then enters his credentials

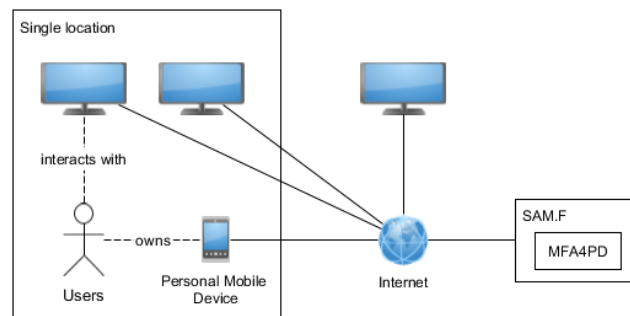


Figure 1. Illustration of the system’s architecture and network.

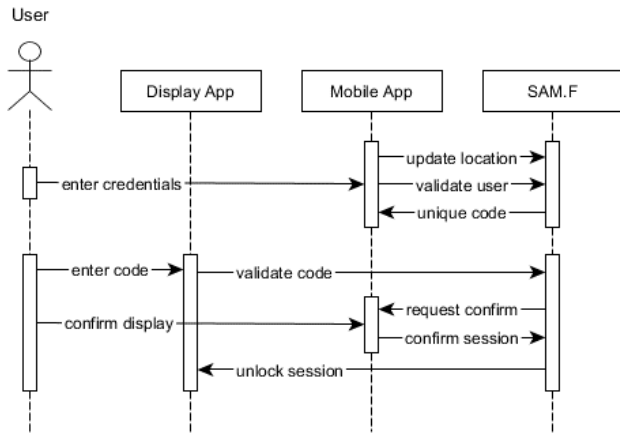


Figure 3. Sequence diagram showing the authentication of one session by a user.

previously registered with SAM.F, which the Web application submits to MFA4PD, as illustrated in Figure 3.

At this point, the process of authentication might be enhanced by further means of MFA, such as gathering biometrical data from fingerprint sensors, facial recognition, or voice sensors. These extensions however might require at least a hybrid application deployment for mobile devices, in order to access the appropriate sensor data. For this reason, in this initial approach, we focused on the Web application combining MFA with ownership and knowledge factors.

The users are identified and authenticated by MFA4PD through their credentials. During the entire process, MFA4PD continues to check the actual location of the user. The location is determined from the GPS data, which is accessible through the smartphone’s Web browser API. If any location mismatch occurs, the process to establish a secure session or the session itself will be terminated immediately for security reasons. This feature might prove useful, whenever a user leaves the location of a public display. However, we did not evaluate this feature’s aspect nor the accuracy required from GPS data in order to work in an everyday scenario, yet.

After the user’s location and credentials are validated, SAM.F generates a code consisting of five symbols, which is shown to the user on his mobile device, as illustrated in Figure 3. The code is valid for a short period of time and the specific user only.

In order to authenticate him- or herself on a public display, the user has to enter the one-time code shown on his smartphone. The user opens up the login dialogue of the *display application* on the public display, and a grid of symbols is displayed. Within this grid, the user now selects the symbols shown on his or her smartphone. The display application communicates the code back to the MFA4PD module, as shown in Figure 3. This serves two purposes:

- a. to identify the display, the user selected from the number of public displays available, and
- b. to identify the user, who chose a public display.

However, the session is not yet usable. The last step to enable the session on the public display requires the user to

again interact with his smartphone in using the *confirm mechanism*. As illustrated in Figure 3, the MFA4PD module sends an authentication request to the mobile application. The dialogue shown indicates a login event took place, together with the name and location shown on the public display. Without the user confirming his or her login on the public display, the session will not be unlocked.

The session on the public display is released after the user’s confirmation using the mobile application.

The users can now put their smartphones away and start using the public display, until they log out.

An additional timeout mechanism prevents misuse of the session on a public display.

The users can also close the session at any time using their smartphones, e.g., in case they forgot to select the logout function on the public display. In addition, SAM.F monitors the users’ location throughout the entire process and session in order to prohibit misuse of login or automatically logout a session after a user clearly left the screens location.

Now that the systems architecture and concept have been illustrated, in the following section, this approach is viewed with regard to security.

### C. Security

As outlined above, related work identifies possible means to attack public display authentication, such as shoulder surfing attacks (a), thermal attacks (b), or smudge attacks (c).

Combining ownership and knowledge factors together with the confirm mechanism, only initially entering the user credentials on the mobile application is vulnerable to shoulder surfing attacks. However, once the trust relationship is established between SAM.F and the users’ smartphone for the current location, another mobile application login is prohibited for the duration of that trust membership.

In our prototype, we use session cookies and device cookies to temporarily store trust relationship data. In future work, we will improve and further enhance security, possibly by integrating the Web application into a hybrid application. This way, the device ownership factor is strengthened. In hybrid applications it will be possible, e.g., to read the device’s hardware id and bind session.

With regard to the one-time code displayed on the mobile application, as well as the user’s input of this code on the display application, they are not vulnerable to shoulder surfing attacks. Again, the confirmation mechanism protects the theft of the session. If any irregularity occurs, the user just declines unlocking the session and generates a new code.

If a user accidentally confirms a session for a code that was used on another display or by anyone else, the simplest way is to just close the session from the user’s smartphone immediately. However, this case is unlikely to occur due to the one-time code concept and the narrow time frame in which a code can be used.

Both thermal attacks and smudge attacks cannot be used on public displays in this approach. Once the one-time code has been used, it is invalidated. The statistical possibility of guessing a one-time code can be decreased by a higher

number of symbols used in the one-code, a larger symbol inventory, or a larger grid.

The users are identified and authenticated by MFA4PD through their credentials. During the entire login process and, in concept, during the entire authenticated session, MFA4PD continues to check the user's location. The location is determined from the GPS data, which is accessible through the smartphone's browser API. If any location mismatch occurs, the process to establish a secure session is aborted. Also, in theory, any ongoing session will be terminated immediately for security reasons. This feature might prove useful in case a user leaves the location of a public display without logging out. However, the evaluation of this feature or the accuracy required from GPS data in order for this concept to work in an everyday scenario will be carried out in future work. For Android and iOS devices, we note that continuously monitoring the user's location requires background activity privileges for an application, which a Web browser application usually does not have. Thus, to enhance security by these means currently requires implementing a hybrid app for smartphones.

In summary, with regard to security, the system's concept offers protection against shoulder surfing attacks, thermal attacks, or smudge attacks. In future work, we will also address the question of whether the server can be compromised. We will also focus on possible security issues with regard to client-server communication, in this case the communication between the display application, the mobile application and SAM.F.

#### D. Prototype Implementation

The prototype consists of three components: (1) the MFA4PD module extending the services of SAM.F, (2) the mobile application and (3) the display application.

SAM.F is developed as Internet Information Services (IIS) application for Windows Servers, as outlined above. The MFA4PD module is implemented as ASMX Web service and a backend-only application, which adds an ASMX Web service to the framework and interfaces with SAM.F.

The mobile application is also developed as IIS application and interfaces with the MFA4PD service. It consists from an ASPX form using JavaScript and AJAX to interact with the frameworks service, whereas the graphical user interface can be customized using HTML and CSS.

The display application consists of a graphical component including the necessary HTML, CSS and JavaScript code. It interfaces with the MFA4PD module via JavaScript through AJAX. The display application also comes with a lightweight backend for session management, that also interfaces with the MFA4PD module. This is currently implemented in ASP.NET.

In order to incorporate the display application into an existing application, we provide code snippets that can be integrated into any application. If a target project does not run ASP.NET, the required server-side code can be translated for other frameworks.

We plan to make the prototype available for non-commercial use later this year.

#### E. Results and Future Work

We tested the prototype under laboratory conditions with mobile devices running Android with Firefox, Edge and Chrome Web browsers. In all tests, we were able to complete the authentication process. However, an evaluation in an everyday setting with a heterogenic group of users is still pending. In addition, the system still has to be evaluated quantitatively with a larger number of users, for example with regard to system's performance, usability, the user's acceptance, or security.

In order to detect if user's change their location, we currently detect their GPS position through the Web browsers API on their mobile device. We have not evaluated the accuracy of this feature as part of this work. Known issues using this approach are, e.g., the lack of accuracy of GPS in buildings, or that this approach cannot be used under lock screen mode of smartphones. Although the latter issue may be resolved by using a hybrid app, we will also look at other approaches to detect if users leave the location of the public display without logging out of their session, without using additional hardware in the installation next to the public display.

#### V. CONCLUSION

Public display authentication is vulnerable to various attacks and technically presents a challenge, whenever public displays are connected to protected networks that are inaccessible for other devices and public displays are not equipped with dedicated user authentication hardware.

In this contribution, we present a technical solution we developed at the Kingsbridge Research Center (KRC), which addresses these challenges with a minimal technical solution. This makes use of a multi-factor authentication (MFA) applying the factors of ownership, knowledge and location. Not requiring any hardware upgrades for public displays, the solution implemented as a prototype makes use of the personal mobile devices of users, connecting them, as well as public displays to the Semantic Ambient Media Framework (SAM.F). Through a dedicated Web service module multi factor authentication is provided for public displays in three steps. In the first step, the user is authenticated using his smartphone. In the second step, the user enters a one-time code on the public display, which is displayed on his smartphone. In the third and final step, the user confirms his session on that particular private display on his smartphone.

In the first prototype, authentication on the smartphone is carried out by entering a username-password combination.

Although this work does not focus on implementing more factors at this stage, together with the knowledge factor, the system can be extended with *biometrical* factors, using supplementary sources for multi-factor authentication, such as fingerprint scanners, facial recognition, or voice biometrics.

We have technically validated our approach under laboratory conditions. In the future, we plan to evaluate the system with a large number of users under everyday conditions, in the best case together with a project partner and by using publicly accessible public displays. Research

questions in this area also relate to the degree of security measures, that users are willing to accept in their everyday dealings with digital systems, as well as the question of how they perceive security issues with regard to their use of personal and private data and contexts on public displays.

The Kingsbridge Research Center is a non-profit research company based in Hamburg, Germany. With our research it is one of our goals to strengthen the use of digital technology in public environments in our digital society. We achieve this goal through our scientific and project-oriented work. Currently, our non-profit activities and the development of new future-oriented projects is funded privately. At a time, when many are confronting digitization with skepticism and uncertainty, we are committed to communicating security in the mindful use of these technologies and through fostering awareness.

#### REFERENCES

- [1] T. Kubitzka, S. Clinch, N. Davies, and M. Langheinrich, 'Using Mobile Devices to Personalize Pervasive Displays', *SIGMOBILE Mob Comput Commun Rev*, vol. 16, no. 4, pp. 26-27, Feb. 2013.
- [2] A. Ometov et al., 'Multi-Factor Authentication: A Survey', *Cryptography*, vol. 2, pp. 1-31, 2018.
- [3] M. Eiband, M. Khamis, E. von Zezschwitz, H. Hussmann, and F. Alt, 'Understanding Shoulder Surfing in the Wild: Stories from Users and Observers', in *Proceedings of the 2017 CHI Conference on Human Factors in Computing Systems*, New York, NY, USA, 2017, pp. 4254-4265.
- [4] Y. Abdelrahman, M. Khamis, S. Schneegass, and F. Alt, 'Stay Cool! Understanding Thermal Attacks on Mobile-based User Authentication', in *Proceedings of the 2017 CHI Conference on Human Factors in Computing Systems*, New York, NY, USA, 2017, pp. 3751-3763.
- [5] K. Mowery, S. Meiklejohn, and S. Savage, 'Heat of the Moment: Characterizing the Efficacy of Thermal Camera-based Attacks', in *Proceedings of the 5th USENIX Conference on Offensive Technologies*, Berkeley, CA, USA, pp. 6-6, 2011.
- [6] E. von Zezschwitz, A. Koslow, A. De Luca, and H. Hussmann, 'Making Graphic-based Authentication Secure Against Smudge Attacks', in *Proceedings of the 2013 International Conference on Intelligent User Interfaces*, New York, NY, USA, 2013, pp. 277-286.
- [7] M. Khamis, R. Hasholzner, A. Bulling, and F. Alt, 'GTmoPass: Two-factor Authentication on Public Displays Using Gaze-touch Passwords and Personal Mobile Devices', in *Proceedings of the 6th ACM International Symposium on Pervasive Displays*, New York, NY, USA, 2017, pp. 8:1-8:9.
- [8] Eurostat, 'Internet use by individuals', 260/2016, Dec. 2016.
- [9] D. Bouck-Standen, 'Introducing SAM.F: The Semantic Ambient Media Framework', in *AMBIENT '19*, Porto, Portugal, *In Press*, 2019.
- [10] P. A. Shaw, M. A. Mikusz, P. T. Nurmi, and N. A. J. Davies, 'Tacita-A Privacy Preserving Public Display Personalisation Service', *UbiComp 2018*, pp. 448-451, 2018.
- [11] N. Memarovic, I. Elhart, A. Michelotti, E. Rubegni, and M. Langheinrich, 'Social Networked Displays: Integrating Networked Public Displays with Social Media', in *Proceedings of the 2013 ACM Conference on Pervasive and Ubiquitous Computing Adjunct Publication*, New York, NY, USA, 2013, pp. 55-58.
- [12] M. Mannan and P. C. van Oorschot, 'Using a Personal Device to Strengthen Password Authentication from an Untrusted Computer', in *Financial Cryptography and Data Security*, Berlin, Heidelberg, 2007, pp. 88-103.
- [13] D. Bouck-Standen, 'Construction of an API connecting the Network Environment for Multimedia Objects with Ambient Learning Spaces', Master Thesis, 2016.
- [14] D. Bouck-Standen et al., 'Reconstruction and Web-based Editing of 3D Objects from Photo and Video Footage for Ambient Learning Spaces', *Int. J. Adv. Intell. Syst.*, vol. 11, pp. 91-104, 2018.